High-Speed Optical Mode Switch Using Refractive Index Change Based on Current Injection

リアン, イマンシャ

High-Speed Optical Mode Switch Using Refractive Index Change Based on Current Injection

Interdisciplinary Graduate school of Engineering Science, Kyushu University
Hamamoto Laboratory
August, 2018

Ryan Imansyah

Abstract

Conventional electrical router experiences a severe problem in power consumption especially for sustaining the future demand of data traffic. Optical switch is attractive because it will decrease the power consumption of the router by eliminating the optical-electrical-optical (OEO) signal exchange. One of the optical switch is based on Si-wire waveguide, known as the optical spatial switch. One of the advantage by using Si-wire waveguide is the possibility to realize revolution of on-chip communication. Moreover, silicon photonics can deliver dense footprint and also nanosecond scale reconfiguration time using electro-optic phase shifter. However, scalability for high integration of this optical switch become the main challenges to realize the optical switching. It works based on the optical input and output ports, thus, it needs the S-bend region for fiber array connection although the dimension of switching element is reduced by the latest silicon photonics technology. To overcome this issue, we proposed optical mode switch.

Optical mode switch can be realized because the optical mode that is orthogonal with each other can be mux/demux. Differently with the optical spatial switch, it only requires a single few-mode fiber (FMF) or multi-core fiber (MCF) connection in the both input and output port. Thus, the matrix size limitation issue of the high integration in the optical spatial switch can be

improved. So far, we have demonstrated the device principle by utilizing the passive device.

The electrically controlled mode switch has been demonstrated with the mode crosstalk of approximately -10 dB for 1550 nm wavelength with the injection current of 60 mA (5.7V) for the TE mode. While the mode-switching time of 2×2 silicon optical mode switch by using p-i-n trench structure was 40 ns for first order mode to fundamental mode, and a switching time of 60 ns for fundamental mode to first order mode. This switching time can be improved by optimize the p-i-n trench structure as the main part to shift the phase of the fundamental mode in one of the arms. The improvement can be done by optimize the trench dimension, increasing the dose level, and optimize the implantation energy.

Acknowledgments

First and foremost, I want to thank my supervisor Prof. Kiichi Hamamoto for the acceptance to be his student and the continuous support of my study in Kyushu University since I took my Master until I finished my Ph.D. He has taught me, both consciously and unconsciously, how the experiment of optical mode switch is done. I appreciate all his contributions of time and ideas to make my Ph.D. experience productive and stimulating. I am also thankful for his help to start the career after I finished the study in Kyushu University.

I want also to thank my co-supervisor Prof. Haisong Jiang for the guidance and help to accomplish my study in Kyushu University. With her kindness and patient, she has helped me in so many ways for my study and experiments. I am also thankful for the excellent example of multilingual person, it motivates me to be fluent in Japanese and learn other languages.

Besides my supervisor and co-supervisor, I would like to thank the rest of my thesis committee: Prof. Kiichiro Uchino and Prof. Kazutoshi Kato, for their insightful comments and encouragement, but also for the question wich incented me to widen my research from various perspective.

I also want to thank my lab rotation supervisors: Prof. Hiroshi Nakashima and Prof. Shiyoshi Yokoyama, for accepting me to be a part of their students for a couple months. It gave me another experience to broaden my

knowledge in this field.

The members of Opto-electronic Hamamoto Laboratory have contributed immensely to my personal and professional time at Kyushu University. The group has been a source of friendships as well as good advice and collaboration. I am especially thankful for the collaboration of Optical Mode Switch group members to do the study and experiment with me : Tatsushi Tanaka, Himbele Luke, Oe Shota, and Satoshi Ogawa. I also want to thank Wenying Li and Bingzhou Hong who came in the same time to Japan with me five years ago, they helped me a lot to survive in Japan with those kanjis that I don`t know. I adore their hard work and motivation. I also want to thank Mr. Yasuhiro Hinokuma for his help to do my experiments and study. My fellow office mates: M. Nassirudin, Ahmad Syahrin, and Mahmoud Nasef. I very much appreciated their kindness, helped, and support during my study, and also their patient towards my noisy and messy table. Other present laboratory members that I have had the pleasure to work with or alongside of are grad students Yu Han and Zanhui Chen; master students Tomotaka Mori, Kantaro Fujimoto, Ryota Kuwahata, and Shingo Murakami; undergraduate students Keisuke Iwasaki and Tomoya Zennoji. I also want to thank the past laboratory member Yutaka Chaen, Hirohito Hokazono, and Kazuhiro Tanabe for their help during my first year in Japan, not to mention their help towards my experiments and study.

For the study in Kyushu University I would like to thank the Green Asia (GA) program, the GA professors: Mr. Andrew Spring, Mr. Keisuke Yamamoto,

Mr. Hiroshi Furuno, and Ms. Naoko Mae, for their guidance during my journey in GA program. Not forget the GA staffs: Ms. Yuko Hayashi, Ms. Yoshiko Kano, Ms. Yu Kazekita, Ms. Ishibashi, Ms. Shiragaki, Ms. Inoue, and Mr. Makino, for their help towards my completion in every activity for GA program. Especially Ms. Yuko Hayashi that helped me a lot to survive in Japan including preparing the things for getting a job, improving my Japanese skill, and her suggestion in a hard time.

My time at Kyushu University was made enjoyable in large part due to the many friends and groups inside and outside Kyushu University that became a part of my Life. I am grateful for time spent with them, Su Liwen, my twin sister different parents. Alisa Banaron, we just known each other less than 3 years yet feels like already a decade. The GA students in the same batch: Zayda Faizah Zahara, Azizah Intan, Sendy Dwiki, and Pennapa Tungjirattitikan, it's such a journey to complete the study with you. The fellow Indonesian students: Dalton, Ayu, Halim, Adit, Etika, Aam, and Aji, for the kindness that made Japan feels like home. The Thai students that I always had the lunch together: Kurrapha, Iize, and Phum, for the talks and laughs during lunch. My friends other friends that I met in Japan: Riya, Farina, Hong, David, John, Radit, Hiroko, and Howard. Thank you for your support and the time that we spent and making my life more colorful. Not to forget as well my grateful to all my best friends in Indonesia: Melissa, Ardhini, Chairul, Nalendra, Diatri, Andika, and Via.

Lastly, I would like to thank my family for all their love and

encouragement. For my parents who raised me with a love, always praying for me, and supported me in all my pursuits. For my sister and her husband who always taking care my parents while I was not presence at home during my study. My nephew and niece who gave me a reason to work hard and do my best. The Yusuf family and Dirmansyah family who always supporting me and praying for me. Thank you.

Ryan Imansyah
Kyushu University
August 2018

Table of contents

Chapter 1

Introduction

The rise of cloud computing and other web applications induces data storage to be centralized in data centers. This idea of using data centers to form a seamless infrastructure capable of running applications and storing data remotely will make the Internet Protocol (IP) traffic to grow exponential pace continuously. It is following the proliferation of smart mobile devices and driven by increasing demands for multimedia, video-on-demand, and other data services [1,2]. It makes Data Center (DC) networks are suffering from the growing demands, various applications and virtualization trends [3-5].

This condition has created the communication traffic to/from data center getting higher, the demand of interconnection network in data centers increased, and also more powerful large-scale of data centers is needed. It is expected that the projected future interconnection network traffic cannot be sustained without consuming the excessive amount of power. Thus, the data center need to be improved in order to support the very large scales of internet traffic while also keep the footprint and lower the power consumption. To overcome these problems due to the hardware limitations of electrical DCs, optical switching has been investigated in several projects to realize the all-optical networks [6-8].

The objective of this thesis is to develop the all-optical network system for data centers that can follow the internet connection traffic trends while

keeping the low scale and higher energy efficiency. Following the ongoing research of data center network design, we aim to use the mode division multiplexing (MDM) for the scalability and energy efficiency improvement.

1.1 Background: Challenges of the present data center networking

The recent DCs are organized in a multi-tier topology where the electronic switches are used for the interconnection between groups of servers and top-of-rack (ToR). However, there is a limitation of I/O bandwidth due to the use of a ball grid array (BGA) in the hardware package [9]. Moreover, by using the conventional electronic switches, optical-to-electrical and electrical-to-optical (OEO) converter is needed, which leads to high power consumption, limited scalability, and also high latency.

1.1.1 high power consumption

The excessive amount of power consumption is one of the most challenging to maintain the demand of future internet traffic. The estimation from a green peace report said that the global demand for electricity from data centers will be triple from 330 billion kWh in 2007 to more than 1000 billion kWh in 2020 [10]. Fig 1 shows the breakdown of energy consumption by different components of a data center [11]. It shows that server and storage and also network hardware spend 26% and 10% of the total power, respectively. The network seems only spent 36% of the total power, however, the electronic and switch in the

conventional data center taking part for the consumption from the cooling system. A single switch in higher data center network tiers can consume more than ten kilowatts if cooling system also being considered [12].

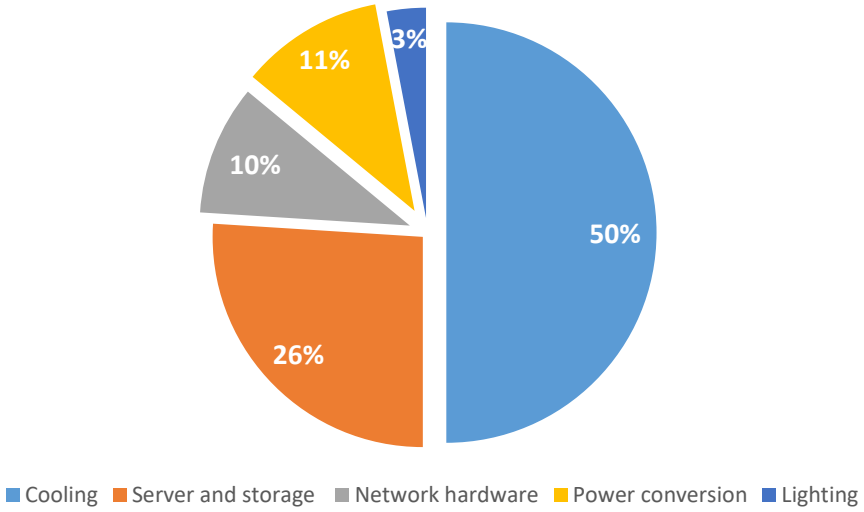

Fig. 1. A breakdown of energy consumption by different components of a data center [11]. Most of the cooling is needed for the electronic and switch part of the data center.

1.1.2 Limited scalability

According to Cisco, the annual global data center will reach 20.6 Zettabytes (ZB) or 1.7 ZB per month by the end of 2021, up from 6.8 ZB per year or 568 exabytes (EB) per month in 2016 [13]. However, the architecture based on Ethernet links and switches has a limited capacity to manage this traffic flowing within data centers. The data center network also will be hard pressed by the technology trends and seems

that the Moores's law seems to be applicable to increase the performance for the near future [14].

1.1.3 Space management

In order to follow the demand of future internet traffic, nonblocking data center connectivity is needed. It would require a massive amount of Ethernet cables when the data center should accommodate millions of server cores [14]. It will lead to severe implementation, management, and maintenance problems.

1.1.4 High latency

The conventional routers yield a relatively high and variable latency or delay, thus, it is not capable of supporting many multimedia applications. Which means they are also incapable to operate at the gigabit speeds. Meanwhile, the oversubscription ratio is increased rapidly. Oversubscription is defined as the ratio of the worst-case achievable aggregate bandwidth among the end hosts to the total bisection bandwidth of a particular communication topology [15]. For examples, servers are able to communicate within the rack at the full rate of their interfaces [14]. Uplink from ToRs are typically 5:1 to 20:1 oversubscription, or 2 to 8 Gbps uplink for 40 servers [16]. Paths through the highest layer of the tree may even be 240:1 oversubscribed [16, 17].

1.2 Proposed solution: optical mode switch for faster switch and scalable architecture

To overcome these problems due to the hardware limitations of electrical DCs, optical switching has been investigated in several projects to realize the all-optical networks [6-8]. The purpose is to overcome the power issue and electrical-to-optical (OEO) signal exchanges problem in the conventional router, OEO switching process has a low latency of ns order switching [18]. There are three major properties of optical transmission technology: ultra-high capacity, low power consumption, and small footprint.

1.2.1 Ultra high capacity

One of the problems in optical signal processing is the capacity of single-mode fiber that almost reaches the physical limit of 100 Tb/s. There are several digital signals processing (DSP) method that can accommodate the explosive growth of data communication traffic. These methods are Time Division Multiplexing (TDM), Spatial Division Multiplexing (SDM), Wavelength Division Multiplexing (WDM) and Mode Division Multiplexing (MDM). These techniques can be realized by using the multi-core fibers (MCF) and multi-mode fibers (MMFs) as a form of multi-input multi-output (MIMO) transmission [19-21].

1.2.2 Low power consumption

Low power consumption is one of the major characteristics of optical links and switches [22-24]. Optical switching technology has a power efficient because of the bit rate transparency, which means it

consumes power independent of the bandwidth of the signal it switches [14]. As the result, power per unit bandwidth in optical switches could be lower than the electronic switches.

1.2.3 Small footprint

A fiber optic has only a diameter of 125 μm, however, it has a significant capacity to provide. Optical switching components could be built very compact through photonic integration [14]. However, minimize the cable installation in the data center architecture is needed in order to make the installation, management, and maintenance more efficient.

In the conventional SDM, optical transmission is currently utilized in data centers only for some point-to-point links on multimode fibers. To extend the capacity a new installation of fiber is needed, however, there are not so many rooms left for it. As already mentioned in 1.2.1, There are several DSP methods that can accommodate the explosive growth of data communication traffic. These methods are attractive because it can be realized by using the MCF and MMFs as a form of MIMO transmission [19-21]. For example, WDM with ring topology is attractive because it doesn't need to be connected with each other while still accommodate a massive data communication traffic. However, to keep increasing the capacity, the MDM combine with WDM has been studied. In here to treat the modes, optical mode switches and add/drop multiplexer are needed. Figure 2 shows the

evolution of router connection architecture. While the add/drop multiplexer is shown in fig. 3.

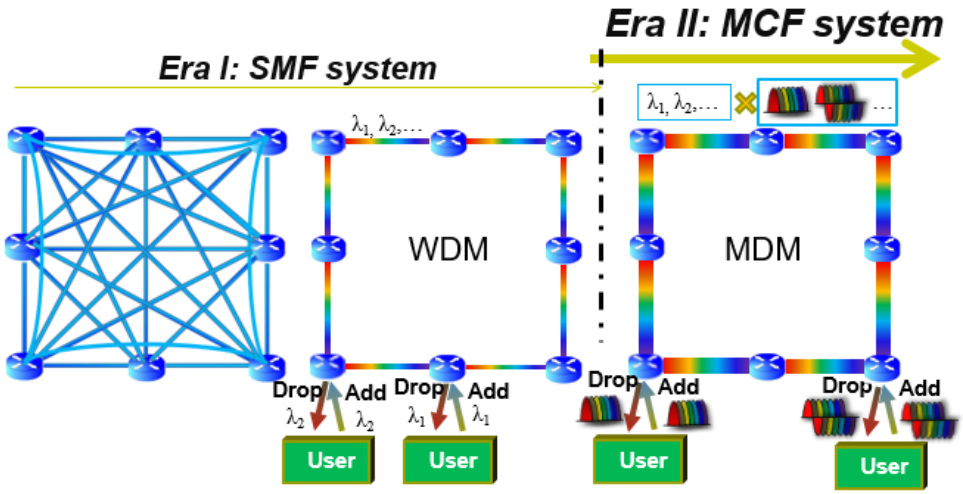

Fig. 2. The evolution of router connection architecture. The combination of MDM and WDM will increase the capacity of communication traffic.

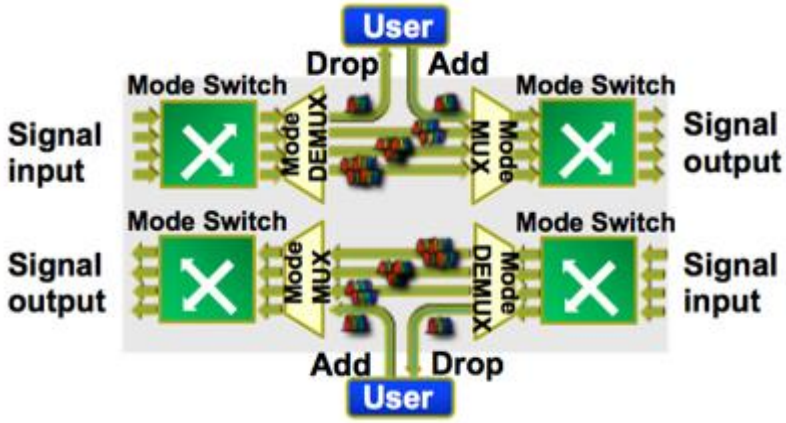

Fig. 3. Add/drop multiplexer in optical mode switch architecture. Add drop is needed to connect each user with the main line of ring topology.

The focus in this research is to design a data center network for the next generation of optical switching by using the MDM with a ring topology. However, there are so many steps to be done to realize this system. In the beginning, the study of optical mode switch is discussed in this thesis.

There are several types of optical switch, optomechanical switches [25], micro-electro-mechanical systems (MEMS) switches [26, 27], electro-optic switches [28], thermo-optic switches [29], liquid-crystal switches [30], bubble switches [31], semiconductor optical amplifier switches [32], and fiber bragg grating based switches [33,34]. The application is different from each other, depends on the needs for a telecommunication system. From all the types of optical switch, waveguide-based optical space switch is more attractive because it can utilize refractive index change that may result in high-speed operation of ns order switching. It is believed that by using the optical switch, can save up to 92 percent space and 96 percent power [35].

However, the switch matrix size issue occurs on waveguide type optical space switch due to the bending waveguide region to open up toward array fiber. This problem occurs because normally it has an adjacent spacing of 125 µm, even if the size of switching elements is reduced by the latest advanced waveguide technologies including wire waveguide, silicon photonics, and photonic crystal. The other problem is the fiber nesting that is occurred because we need a lot of input port and the output port. In order to overcome the fiber nesting and the switch matrix problems in optical switching, we proposed the optical mode switch.

1.3 Optical mode switch: state of the art

Compared to a conventional optical spatial switch, the optical mode switch only needs one input and output port by employing a few-mode fiber (FMF) or a multicore fiber (MCF). A number of optical modes switches have been reported, such as the one driven by electromagnetic field [36], thermos-optically tuning waveguide with Mach-Zehnder Interferometer (MZI) structure [37], electro-optic grating Lithium Niobate (LN) waveguide [38] and an MZI structure with a phase shifter [39]. The summary of optical mode switch technology is shown in Tab. 1. However, these mode switches suffer from low switching speed, high driving voltage, and large size. On the other hand, Si-wire based optical spatial switch is attractive because of the potential for high-speed operation and low power consumption [40, 41]. Moreover, silicon photonics offers merits of dense footprint and nanosecond reconfiguration time using an electro-optic phase shifter [42, 43]. The Y-junction and multimode interference based on SOI that was done by McGill University group have a high-speed result of the two-mode switch, however, the device is integrated with the 2×2 MMI structure [44]. It makes the output of the device is fundamental modes but in the different output ports. Among these optical mode switches, we fabricated the device that has only one input port and one output port that will simplify the installation method.

Table. 1: Summary of Optical Mode Switch

Year	Total modes	Structure	Length Dimension	Voltage And λ	Switching time	Ref
2013	2	Symmetric Y-junction waveguides	-	-	-	[45]
2014	2	Two mode fibers inside magnetic coil	100 mm	50 V for 1550 nm	-	[36]
2014	2	Mach-Zehnder Interferometer waveguide by using Dow Chemical benzocyclobutene	3.5 mm	-	-	[37]
2015	2	Long-period waveguide grating in lithium-niobate	8 mm	35 V for 1544 nm	-	[38]
2016	2	Mach-Zehnder Interferometer waveguide with one input port and output port.	1.5 mm	5.6 V	40 ns – 60 ns	[46]

2016	2	Lithium-niobate Mach-Zehnder interferometer	24 mm	3 V for 1550 nm	-	[40]
2017	2	Y-junction and multimode interference based on SOI.	0.6 mm	1.22 V for 1550 nm	2.5 ns	[44]

1.4 Thesis construction

This section provides the overview of the later chapters of this thesis. We begin with the study of the available technologies from the research community aiming at resolving the challenges in data center networks. Our technical contribution is followed in three chapters and finally concludes the thesis.

In chapter 2, to realize the optical mode switch, 2 modes optical mode switch is proposed as the preliminary design of the optical mode switch. In this work, the theory of how to realize the optical mode switch will be discussed.

In chapter 3, in this chapter, the mode evaluation theory will be discussed. MMI mode filter was used experimentally. The mode-switching with an injection current of 60 mA (5.7 V) was successfully evaluated with mode-crosstalk of 10 dB at λ=1550 nm for the TE mode.

In chapter 4, the mode switching speed will be discussed. A minimum of less than 60 ns and 40 ns mode switching time for the fundamental mode to first order mode and vice versa, was achieved respectively.

In Chapter 5, the above results have been summarized and clarified about the future view of the proposed waveguide structure.

1.5 References

[1] K. I. Sato and H. Hasegawa, “Optical networking technologies that will create future bandwidthabundant networks," IEEE/OSA Journal of Optical Communications and Networking, vol. 1, no. 2, pp. A81.A93, Jul. 2009.

[2] M. Jinno, H. Takara, B. Kozicki, Y. Tsukishima, Y. Sone, and S. Matsuoka, “Spectrum-e_cient and scalable elastic optical path network: architecture, benets, and enabling technologies," IEEE Communications Magazine, vol. 47, no. 11, pp. 66..73, Nov. 2009.

[3] M. Meeker and L.Wu, “2013 internet trends,” Kleiner Perkins Caufield & Byers, Technical Report (2013).

[4] S. Sakr, A. Liu, D.M. Batista, and M. Alomari, “A survey on large scale data management approaches in cloud environments,” IEEE Com. Sur. & Tut., vol. 3, no. 13, p. 311-336, Sept. 2011.

[5] Cisco Systems Inc., “Cisco global cloud index: Forecast and methodology 2013–2018 white paper,” 2014.

[6] C. Kachris and I. Tomkos, “A Survey on Optical Interconnects for Data Centers,” IEEE Communications Surveys & Tutorials, vol.14, no.4, pp.1021-1036, 2012.

[7] N. Farrington, G. Porter, S. Radhakrishnan, H. H. Bazzaz, V. Subramanya, Y. Fainman, G. Papen, and A. Vahdat, “Helios: a hybrid electrical/ optical switch architecture for modular data centers,” in Proceedings of the ACM SIGCOMM 2010, pp. 339–350, 2010.

[8] X. Ye, Y. Yin, S. J. B. Yoo, P. Mejia, R. Proietti, and V. Akella, “DOS: A scalable optical switch for datacenters,” in Proceedings of the 6th ACM/IEEE Symposium on Architectures for Networking and Communications Systems, ser. ANCS ’10, pp. 24:1–24:12, 2010.

[9] A. Ghiasi, “Is there a need for on-chip photonic integration for large data warehouse switches,” Proc. 9th IEEE Int. Conf. Group IV Photon., San Diego, CA, pp. 27-29, Aug. 2012.

[10] Greenpeace International, “Make IT green: cloud computing and its contribution to climate change." [Online]. Available: http://www.greenpeace.org/, Mar. 2010.

[11] Info-Tech, “Top 10 energy-saving tips for a greener data center,” Info-Tech Research Group, London, ON, Canada, Apr. 2010. [Online]. Available: http://static.infotech.com/downloads/samples/070411_premium_oo_green dc_top_10.pdf

[12] W. Zhang, H. Wang, and K. Bergman, “Next-generation optically-interconnected highperformance data centers," IEEE/OSA Journal of Lightwave Technology, vol. 30, no. 24, pp. 3836-3844, Dec. 2012.

[13] Cisco global cloud index: “forecast and methodology, 2016-2021." [Online]. Available: http://www.cisco.com/, Apr. 2017.

[14] H. Rastegarfar, “Optical Switching in Next-Generation Data Centers,” Thesis paper, University of Toronto, 2014.

[15] M. Al-Fares, A. Loukissas, and A. Vahdat, “A scalable, commodity data center network architecture," in ACM SIGCOMM'08, pp. 63.74, Aug. 2008.

[16] A. Greenberg, J. R. Hamilton, N. Jain, S. Kandula, C. Kim, P. Lahiri, D. A. Maltz, P. Patel, and S. Sengupta, “VL2: a scalable and exible data center network," in ACM SIGCOMM'09, vol. 39, pp. 51{62, Aug. 2009.

[17] K. Nagaraj, H. Khandelwal, C. Killian, and R. R. Kompella, “Hierarchy-aware distributed overlays in data centers using DC2," in Fourth International Conference on Communication Systems and Networks (COMSNETS), pp. 1.10, Jan. 2012.

[18] J. V. Campenhout, William M. J. Green, S. Assefa and Y. A. Vlasov, “Low-power, 2x2 silicon electro-optic switch with 110-nm bandwidth for broadband reconfigurable optical networks,” Opt. Express, vol. 17, No. 26, pp. 24020-24029, 2009.

[19] T. Morioka, Y. Awaji, R. Ryf, P. J. Winzer, D. Richardson, and F. Poletti, "Enhancing optical communications with brand new fibers," IEEE Commun. Magazine, vol.50, no.2, pp. s31-s42, Feb. 2012.

[20] P. J. Winzer and G. J. Foschini, “MIMO capacities and outage probabilities in spatially multiplexed optical transport systems,” Opt. Express., vol. 19, no. 17, pp. 16680–16696, Aug. 2011.

[21] R. Essiambre and R. W. Tkach, "Capacity Trends and Limits of Optical Communication Networks," Proc. of the IEEE , vol.100, no.5, pp.1035-1055, May 2012.

[22] D. A. B. Miller, “Device requirements for optical interconnects to silicon chips," Proceedings of the IEEE , vol. 97, no. 7, pp. 1166.1185, Jul. 2009.

[23] A. Shacham, K. Bergman, and L. P. Carloni, “Photonic networks-on-chip for future generations of chip multiprocessors," IEEE Transactions on Computers , vol. 57, no. 9, pp. 1246.1260, Sep. 2008.

[24] S. J. B. Yoo, “Optical packet and burst switching technologies for the future photonic Internet,"IEEE/OSA Journal of Lightwave Technology , vol. 24, no. 12, pp. 4468.4492, Dec. 2006.

[25] S. Nagaoka and Y. Suzuki, “Compact optomechanical switches and their applications in optical communication and testing systems,” in Proceedings of MEMS 1997, IEEE, pp. 366-371.

[26] D. J. Bishop, C. R. Giles, and S. R. Das, “The rise of optical switching,” Sci. Amer., vol. 284, no. 1, pp. 88–94, Jan. 2001.

[27] J. E. Ford, “Optical MEMS: Legacy of the telecom boom,” in Proc. Solid State Sensor, Actuator and Microsyst. Workshop, Hilton Head, SC, Jun. 6–10, pp. 1–3, 2004.

[28] Z. L. Samson, K. F. MacDonald, F. De Angelis, B. Gholipour, K. Knight, C. C. Huang, E. Di Fabrizio, D. W. Hewak, and N. I. Zheludev, “Metamaterial electro-optic switch of nanoscale thickness,” Applied Physics Letters 96, 2010.

[29] E. A. Camargo, H. M. H. Chong, and R. M. De La Rue, “2D photonic crystal thermo-optic switch based on AlGaAs/GaAs epitaxial structure,” Optic Express 12, 4, pp. 588-592. 2004.

[30] Riza, N.A. and S.F. Yuan, “Reconfigurable wavelength add-drop filtering based on a Banyan network topology and ferroelectric liquid crystal fiber-optic switches.” IEEE Journal of Lightwave Technology, 17(9): p. 1575-1584, 1999.

[31] Jackel, J.L., J.J. Johnson, and W.J. Tomlinson, “Bistable Optical Switching Using Electrochemically Generated Bubbles,” Optics Letters, 15(24): p. 1470-1472, 1990.

[32] Renaud, M., M. Bachmann, and M. Erman, “Semiconductor optical space switches,” IEEE Journal of Selected Topics in Quantum Electronics, 2(2): p. 277-288, 1996.

[33] Ball, G.A. and W.W. Morey, “Tunable Bragg grating fiber filters and their applications,” in Conference on Lasers and Electro-Optics (CLEO). 1997.

[34] Melloni, A., M. Chinello, and M. Martinelli, “All-optical switching in phase-shifted fiber Bragg grating,” IEEE Photonics Technology Letters, 12(1): p. 42-44, 2000.

[35] Laura, “ABCs of optical switch,” Fiber optic equipment solutions, FS.com, May 27, 2016. [online]. Available : http://www.fiber-optic-equipment.com/abcs-of-optical-switch.html

[36] H. Sakata, H. Sano, and T. Harada, “Tunable mode converter using electromagnet-induced long period grating in two-mode fiber,” Opt. Fiber Technol., vol.20, no.3, pp.224–227, 2014.

[37] W.Y. Chan and H.P. Chan, “Reconfigurable two-mode mux/demux device,” Opt. Express, vol.22, no.8, pp.9282–9290, 2014.

[38] W. Jin and K.S. Chiang, “Mode switch based on electro-optic long-period waveguide grating in lithium niobate,” Opt. Lett., vol.40, no.2, pp.237–240, 2015.

[39] M. Zhang, K. Chen, W. Jin, and K.S. Chiang, “Electro-optic mode switch based on lithium-niobate Mach-Zehnder interferometer,” Appl. Opt., vol.55, no.16, pp.4418–4422, 2016.

[40] T. Barwicz, H. Byun, F. Gan, C.W. Holzwarth, M.A. Popovic, P.T. Rakich,M.R.Watts, E.P. Ippen, F.X. K¨artner, H.I. Smith, J.S. Orcutt, R.J. Ram, V. Stojanovic, O.O. Olubuyide, J.L. Hoyt, S. Spector, M. Geis, M. Grein, T. Lyszczarz, and J.U. Yoon, “Silicon photonics for compact, energy-efficient interconnects [invited],” J. Opt. Netw., vol.6, no.1, pp.63–73, 2007.

[41] H. Yamada, T. Chu, M. Tojo, S. Nakamura, M. Tokushima, Y. Urino, S. Ishida, and Y. Arakawa, “A compact optical switch module with Si-wire waveguides,” 4th IEEE International Conference on Group IV Photonics 2007 (GFPIV2007), pp.119–121, 2007.

[42] J. Xing, Z. Li, P. Zhou, X. Xiao, J. Yu, and Y. Yu, “Nonblocking 4 × 4 silicon electro-optic switch matrix with push-pull drive,” Opt. Lett., vol.38, no.19, pp.3926–3929, 2013.

[43] B.G. Lee, A.V. Rylyakov, W.M.J. Green, S. Assefa, C.W. Baks, R. Rimolo-Donadio, D.M. Kuchta, M.H. Khater, T. Barwicz, C. Reinholm, E. Kiewra, S.M. Shank, C.L. Schow, and Y.A. Vlasov, “Monolithic silicon integration of scaled photonic switch fabrics, CMOS logic, and device driver circuits,” IEEE J. Lightwave Technol., vol.32, no.4, pp.743–751, 2014.

[44] Y. Xiong, R. B. Priti, and O. L-Ladouceur, “High-speed two-mode switch for mode-division multiplexing optical networks,” Optica., vol.9, no.9, pp.1098-1102,2017.

[45] M. Jizodo, A. Fujino, and K. Hamamoto, “Proposal of Optical Mode Switch Using Symmetric Y-junction Waveguides,” Tech. Dig. IEEE 18th OptoElectronics and Communications Conference held jointly with 2013 International Conference on Photonics in Switching (OECC/PS), pp. 1-2, Kyoto, 2013,.

[46] H. Jiang, R. Imansyah, L. Himbele, S. Oe, and K. Hamamoto, “Fast Mode-Switching (60 ns) by Using a 2×2 Silicon Optical Mode Switch,” IEICE Trans. Electron., vol.E100-C, no.10, pp.782–788, 2017.

Chapter 2

Two Modes Optical Mode Switch Design

2.1 Mode division multiplexing

Mode Division Multiplexing (MDM) is employing the advantage of multi-mode fiber to transmit a different kind of optical modes. The idea is almost the same as Wavelength Division Multiplexing (WDM), however, the source is varied by optical modes. Optical modes can be easily multiplex and demultiplex by using the directional coupler on the silicon-on-insulator platform [1]. However, to optimize the performance of MDM, group delay spread and mode-dependent loss and gain should be considered.

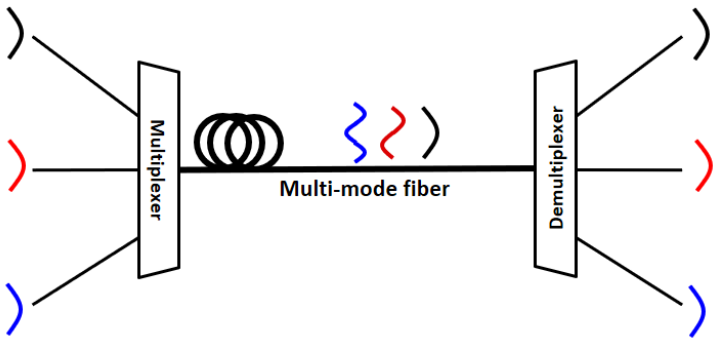

Figure 1. Schematic of MDM with three different modes. It's only need at least one multi-mode fiber in MDM configuration. The modes can be switched by using optical mode switch.

Figure 1 shows the schematic of MDM with three different modes. The signals from multiple senders are transmitted as fundamental mode, however, the signals then propagate as different modes after the multiplexer. Then, the signals are sent to each destination as a fundamental mode with the help of demultiplexer. Thus, by implementing this schematic of MDM, optical mode switch can accommodate both high switching speed and also high capacity of data traffic.

2.2 Device configuration

In order to realize the optical mode switch, high switching speed is not only the important characteristic that needs to be achieved. The high output power is also beneficial in order to get a clear signal transmission. Thus, the device configuration is also needed to be optimize. There are two important parameters for the structure, mode combiner and p-i-n trench structure, in order to optimize the output power of the signals.

2.2.1 Mode combiner

Figure 2 shows a schematic of the optical mode switch for the fundamental-mode and the first-order mode. As shown, the configuration is similar to that of a Mach-Zehnder interferometer, however, there is a difference in the waveguide width of the Y-junction connected to the two single-mode waveguides [2]. Here, we use the symmetric Y-junction that is suitable for equal power splitting [3-6]. The width of the waveguide at the Y-

junction is designed to be twice of the arm's width to realize mode combining for the fundamental mode as well as the first-order mode. On the other hand, to realize mode switching, we designed the symmetrical arms with a refractive index change region in one of the arms. We injected electrical current to this region to generate a π-phase difference between arms.

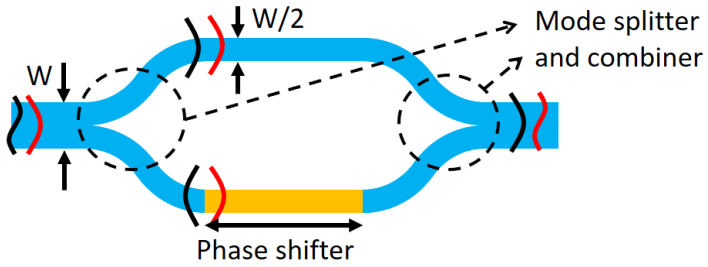

Fig.2. Optical-mode switch configuration. Input and output signals are in the form of fundamental mode and first-order mode with the same input and output port.

When the fundamental mode is injected in the input port, it is going to split into two fundamental modes with the same phase at the 3 dB splitter. While when the first-order mode is injected, it is split into two fundamental modes with phase π difference each other. Figure 2 shows the beam propagation method (BPM) simulation results of the optical mode switch between fundamental mode and first-order mode. When the phase shifter is the bar-state Fig. 3.a, the modes propagate and then couple at the mode coupler into the same modes as the injected modes. When a certain current is injected into the phase shift region and the phase shifter is cross-state Fig. 3.b, the phase of the one split fundamental mode is shifted with π. Thus, these are coupled as the first-order mode at the end. Meanwhile, the injected first-

order mode is converted into the two fundamental modes in the same phase, and then couple as the fundamental mode. Thus, this structure realizes the switching between the fundamental mode and the first-order mode. In such a way, both modes are switched each other simultaneously.

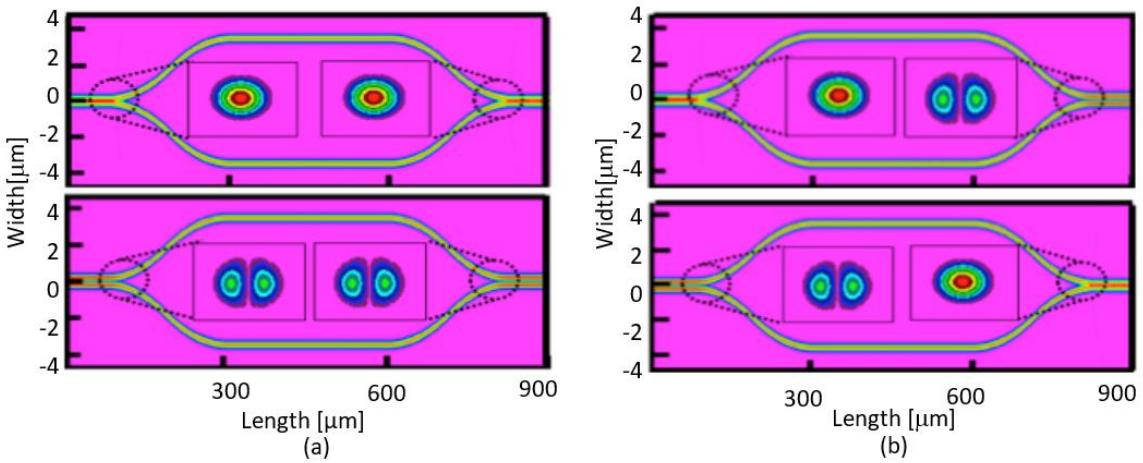

Fig. 3. Simulation results for the (a) bar state and (b) cross state. Bar state shows the condition when there is no π phase shift in one of the arms, while cross state shows the condition when there is a π phase shift in one of the arms.

By injecting the electrical current, the concentration of free charges in silicon changes the refractive index of the material, thus, the phase of the light can be shifted. The relationship between refractive index changes in silicon and the injection of carriers in silicon at 1.55 μm wavelength is expressed by Soref and Bennet using experimental data [7]. This equation is almost universally used for the evaluation of optical modulation in silicon:

$$\Delta n = \Delta n_e + \Delta n_h = -8.8 \times 10^{-22} \Delta N_e - 8.5 \times 10^{-18} (\Delta N_h)^{0.8}, \quad (1)$$

where Δn_e and Δn_h are the changes in the refractive index resulting from the change in free electron carrier concentration (ΔN_e) and free hole carrier concentration (ΔN_h), respectively.

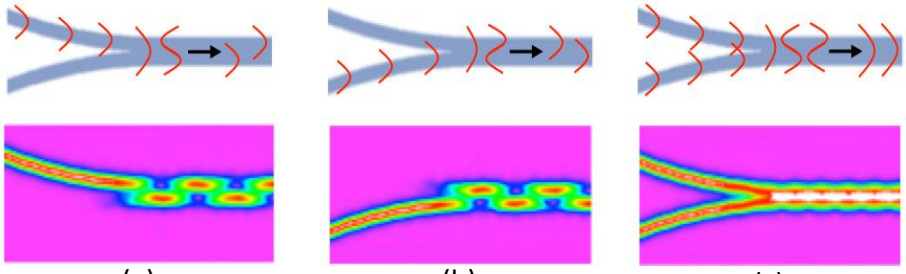

Fig.4. Schematic of the mode combiner and its propagation field for the same phase between arms. (a) Propagation of light from left arm and (b) right arm, and (c) how the lights combine into the fundamental mode after the Y-junction.

Figures 4(a) and 4(b) show the propagation of light in a multimode waveguide after the Y-junction from each arm in the case of the phase of the light at each arm is the same. As shown in the figure, light from one arm propagates in a zig-zag manner [8]. This phenomenon is considered as follows (similar to mode-coupled theory): i) light from one arm is considered as a combination of even and odd modes at the starting point of the multimode waveguide; ii) owing to the propagation constant difference between even and odd-modes, the peak of the combination moves left and right along the direction of propagation; iii) as a result, the light propagates in a zig-zag manner, as shown in Figs. 4(a) and 4(b). This zig-zag propagation occurs for both cases of Fig. 4(a) and 4(b), however, there is the difference between odd modes and even modes. The phases of odd modes in the two arms are

different by π [rad], while they are the same for even modes. Hence, the resulting optical field goes into the regular single mode, as shown in Fig. 4(c).

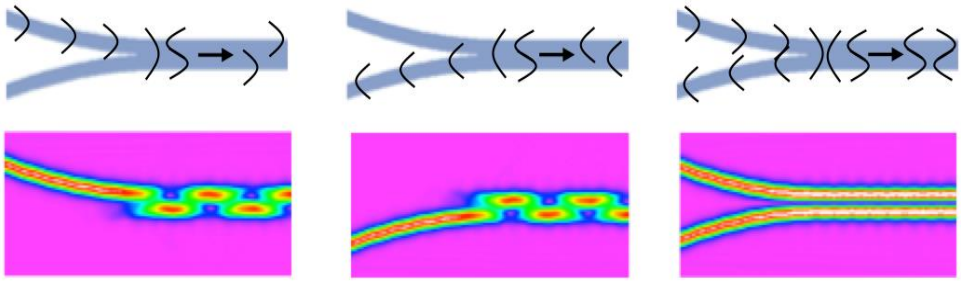

Fig.5. Schematic of the mode combiner and its propagation field for π phase difference between arms. (a) Propagation of the light from left arm and (b) right arm, and (c) how the lights combine into the first-order mode after the Y-junction.

Now, let us consider the case of π phase shift in one arm (Fig. 5). The phenomena that occur at the same Y-junction is considered as follows: i) light from one arm is considered to be a combination of even and odd modes at the starting point of the multimode waveguide; ii) because of the propagation constant difference between even and odd modes, the peak of the combination moves left and right along the direction of propagation; iii) as a result, the light propagates in a zig-zag manner, as shown in Figs. 5(a) and 5(b). This zig-zag propagation occurs in both cases of Figs. 5(a) and 5(b), however, in this case, the phases of “even” modes in each arm are different by π [rad] while the phases are the same for “odd” modes. So, the resulting optical field becomes the first-order mode, as shown in Fig. 5(c).

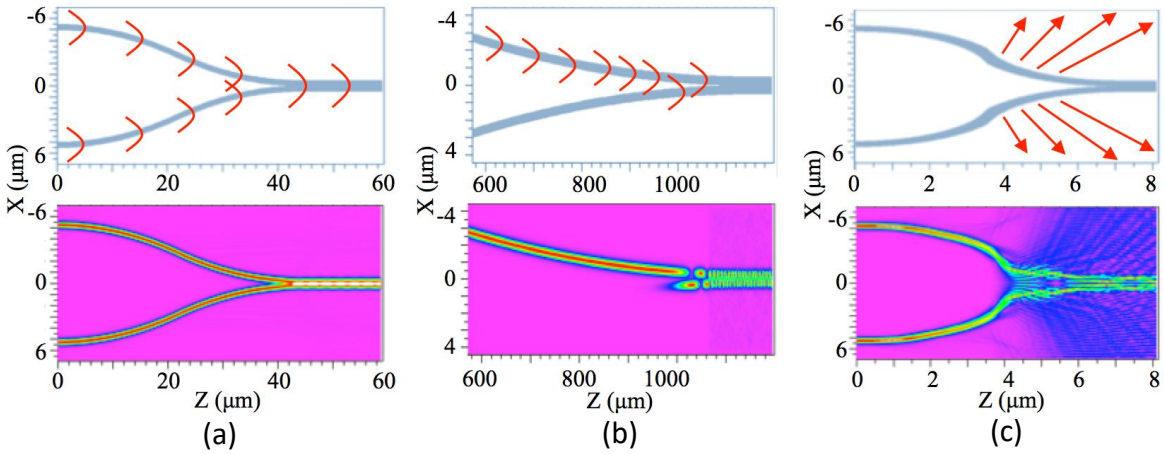

Fig. 6. Schematic and propagation field in mode combiner with the distance between arms of 10 μm: (a) 8 μm < r < 16000 μm, (b) r ≥ 16000 μm, and (c) r ≤ 8 μm. These pictures shows that the undesired coupling when the r is too large and a high loss when it is too small.

To realize a proper mode-combiner based on the Y-junction with two S-bend waveguides as shown in Fig. 6 (a), there may be two critical issues that must be overcome: 1) one is undesired coupling between adjacent waveguides before light propagates into the multimode waveguide, and 2) the other is radiation loss, as explained below.

i. Undesired coupling occurs when bending radius R is too long, as shown in Fig. 6(b). This may degrade the mode. However, the significant undesired coupling is avoided easily when r satisfies r < 16000 μm.

ii. Radiation loss may occur when r is too short [see Fig. 6(c)]. Figure 7 shows the radiation loss as a function of r estimated by the finite domain time difference method (FDTD). Significant radiation is generated when r ≤ 8 μm, as shown in the figure.

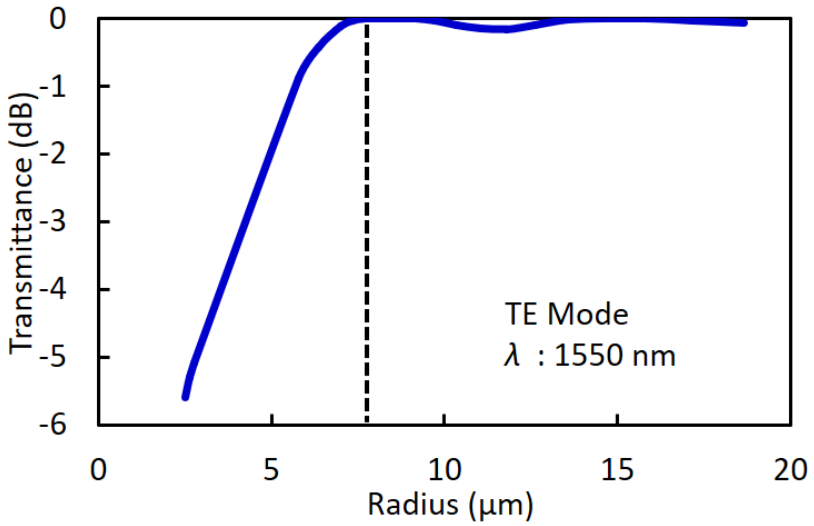

Fig. 7. Output power for short bending radius (r≤ 8 μm) estimated by FDTD method. It shows that above 8 μm, the bending loss is almost zero.

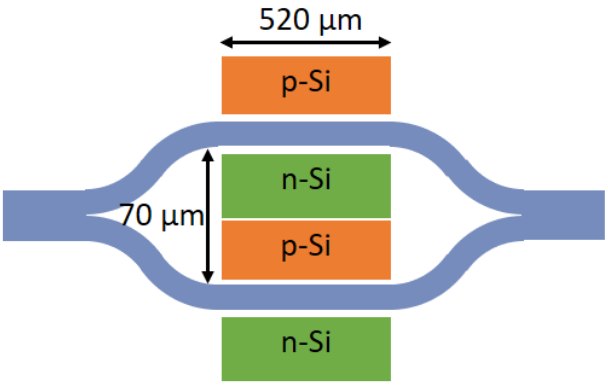

Fig. 8. Opening space of 70 μm for silicon doping between arms of an actual device. This opening space is necessary in order to make the doped region for the phase shifter.

According to these results, the bending radius of 8 μm < r < 16,000 μm is the design criteria for the mode combiner. For the actual device, we designed r to be 610 μm to make a distance of 70 μm between arms for the opening space of ion implantation, as shown in Fig. 8. This distance is used to ensure sufficient space for wire bonding on top of the electrodes.

2.2.2 Trench p-i-n structure

In order to realize the optical mode switch, we fabricated a p-i-n structure in the phase shifter region. In here intrinsic silicon (i-Si) is the waveguide part, thus it is essential to keep the propagation loss low. Thus, p-type and n-type regions must be connected to the waveguide in a lateral direction, as shown in Fig. 9(a), while the other region is fully etched. Thus, at least, a two-step dry etching process is needed. To simplify the fabrication into a one-step etching process, we fabricated a p-i-n trench structure by utilizing the aspect-ratio-dependent etching (ARDE) phenomenon [9, 10]. The silicon etches rate decreases as the open space size decreases. The illustration of wide and narrow open spaces when making a trench structure is shown in Fig. 9(b). A slight amount of the remaining Si layer bridges the p-doped region and the waveguide, as well as the n-doped region and the waveguide, for narrow open spaces. Thus, the p-i-n structure is realized by this technique.

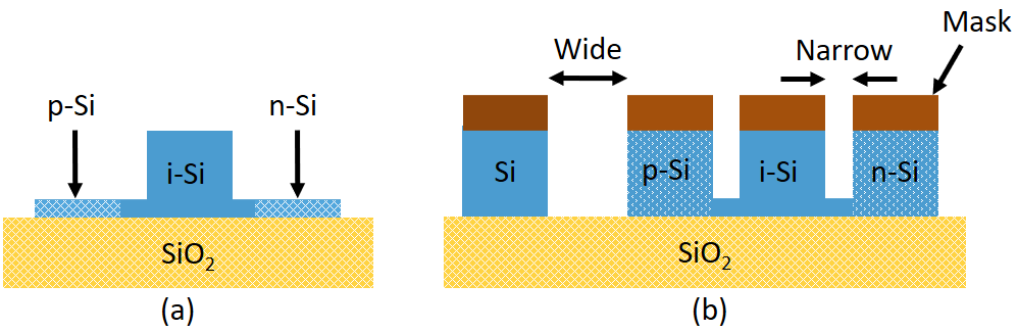

Fig. 9. Cross-section of p-i-n structure. (a) Conventional p-i-n structure and (b) p-i-n trench structure. The narrow opening space has lower etching rate than the wide opening space, thus, two different depths can be made.

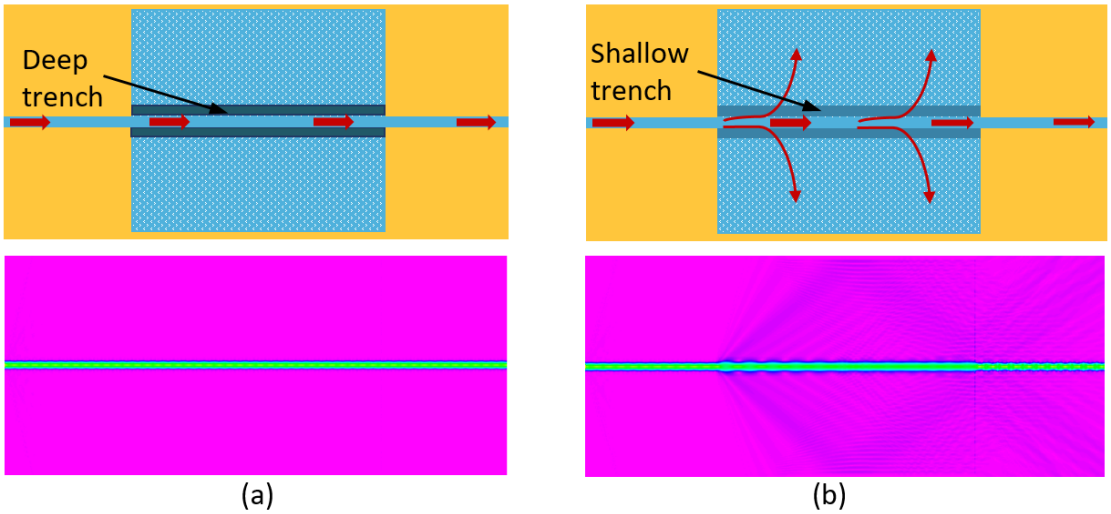

Fig. 10. Propagation field profiles at the trench region. (a) Non-leaky condition and (b) leaky condition. It shows that too shallow trench will increase the propagation loss of the device.

However, one critical issue of the trench structure is its radiation loss toward the trench direction due to the relatively low refractive index contrast in the lateral direction that may cause leaky-mode propagation. Figure 10 shows example propagation field profiles of (a) non-leaky condition and (b) leaky condition at the trench region. As shown in the figure, if the trench region is designed as a leaky condition with a shallow trench, significant radiation happens that causes huge loss while deep trench prevents this radiation as shown in Fig. 10 (b). To side-step this radiation issue at the trench, we verified the design criteria of this region.

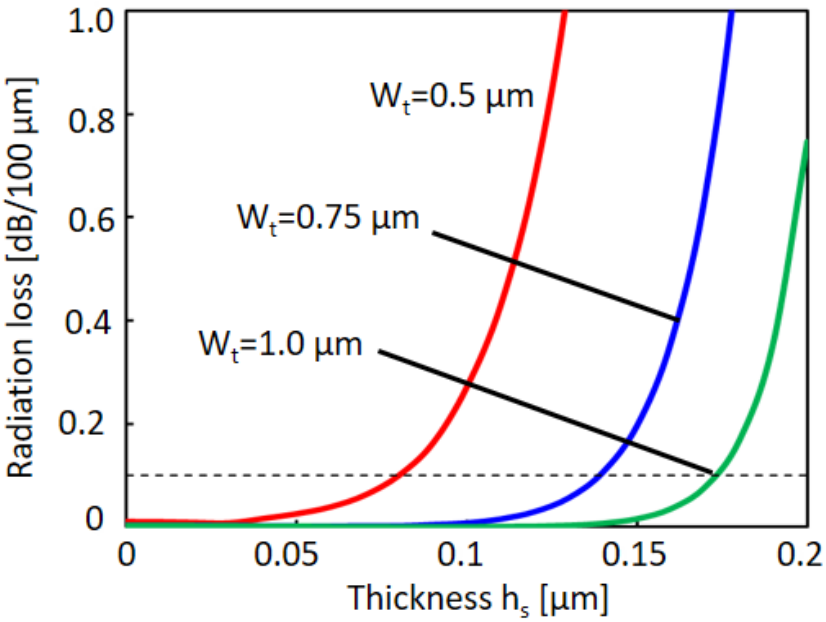

Fig. 11. The radiation loss as a function of thickness of remaining silicon layer. It shows that the narrower of the trench width Wt, the lower fabrication tolerance for the remaining thickness of h_s.

Figure 11 shows the radiation loss as a function of the thickness of the remaining silicon layer h_s. W_t is the trench width and h_s is the thickness of the remaining silicon layer. As can be seen in Fig. 11, the radiation loss is reduced as the trench width W_t increased. When Wt is 0.50 µm and h_s is less than 0.08µm, the radiation loss is suppressed below 0.1 dB/100 µm. The upper limit of h_s increases as W_t increases, thus, manufacturing tolerance is also significantly improved. Based on these design criteria with sufficient fabrication tolerance, we decided to fabricate h_s of 30 nm to suppress the radiation loss with setting W_t to be 0.8µm in this work.

Before we fabricated the p-i-n trench structure, we investigated the etching rate as a function of open space size. We designed two sizes of open

spaces; 0.8 µm and 20 µm, on the basis of silicon-on-insulator (SOI) rib waveguides. The structure was etched using inductively coupled plasma (ICP).

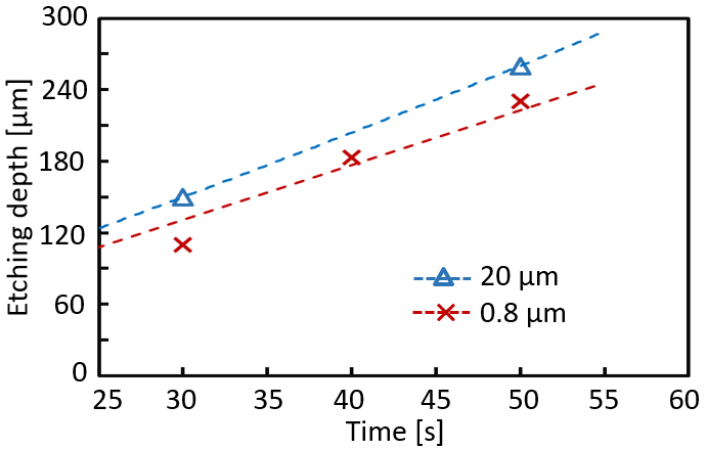

Fig. 12. The etching rate as a function of the opening space size. It shows that the narrow opening space (0.8 µm) has lower etching rate.

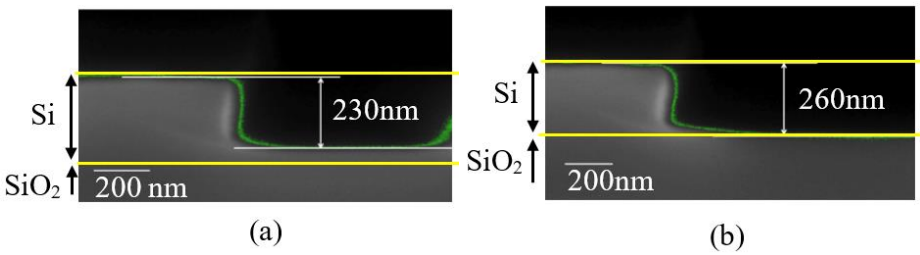

Fig. 13. Trench for p-i-n structure. Cross sections of (a) narrow opening (0.8 µm) and (b) wide opening (20 µm). It shows that a different of 30 nm between narrow opening space and wide opening space can be made in the same etching process.

Figure 12 shows the etching rate as a function of open space size. As can be seen in the figure, the etching rate decreases as the open space size decrease. As shown in Fig. 13(a), 30 nm of Si layer remained as the connector of the waveguide to both the p-doped and n-doped regions after single-step dry etching, because of the etching rate difference.

2.3 Preliminary mode switch using different arm's length structure

In order to verify the basic operation principle of the optical mode switch, cross state device with a different arm's length corresponding to the refractive index conversion region was fabricated on the same substrate. The bar state device with symmetrical arm's length, was also fabricated. These devices were confirmed to be able to inter-mode switching.

To evaluate the mode crosstalk, instead of realizing the phase-shift region based on current injection, we fabricated physical length different devices in the arms [2]. Figure 14 shows the top view of the implemented devices. As can be seen in Fig. 14(a), the device has the same arm length to confirm bar-state. Meanwhile, the device has bending regions in one arm to have a π phase shift between two arms to confirm cross-state. The devices were fabricated using silicon-on-insulator (SOI) wafers with 2 μm thick buried oxide layer (lower cladding layer) and 300 nm top Si layer (core layer).

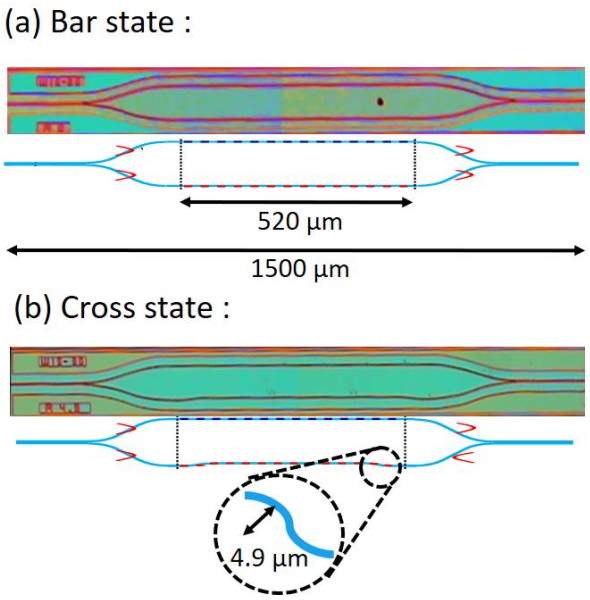

Fig. 14. Top view of (a) symetrical arm and (b) the length different arms device. These device is needed as the preliminary experiment of optical mode switch.

The device was implemented by using inductively coupled plasma (ICP) dry etching technique. At the final process, the surface of the device was covered with SiO_2 using plasma chemical vapor deposition method. The implemented device geometries are summarized in Tab. 1.

Tab. 1 Device geometries

	Dimension
Length	1500 µm
Input output width	3 µm
Arm Width	1.5 µm
Arm Length	520 µm
Radius	4.9 µm
Length different	0.26 µm

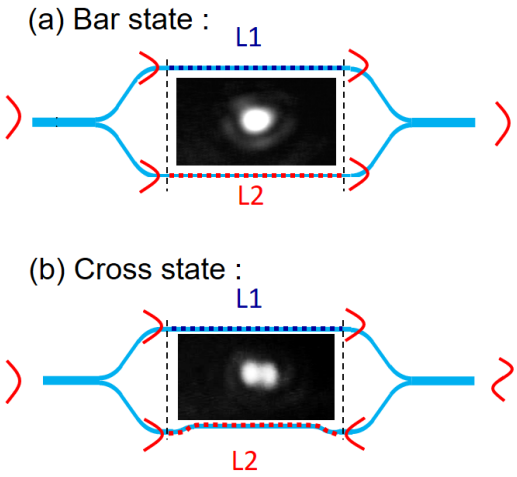

Fig. 15. Waveguide (a) without optical path difference and (b) with optical path difference. It shows the NFP from the bar state and cross state of the device, a clear fundamental and first order mode can be seen from the bar state and cross state, respectively.

Figure 15 shows the near-field pattern (NFP) of the fabricated devices. The injected light was TE fundamental mode light with 1.55μm for both devices. As shown in figure 15(a), the regular fundamental mode was obtained, while regular first-order mode was clearly observed in Fig. 15(b) This result clearly shows that the proposed device principle worked well as the optical mode switch.

2.4 Conclusions

There are two parameters to optimize the optical propagation; the Y-junction Radius r and p-i-n trench structure. The r of the device should be larger than 8 μm to avoid the radiation loss but small enough to keep the small footprint. While in the p-i-n trench structure, the trench width of W_t should be small enough to make the remaining silicon layer thick enough to realize

the plasma dispersion for phase shifting. The p-i-n trench structure was realized by utilizing the aspect-ratio-dependent etching (ARDE) phenomenon. The experiment shows that by setting the open space as 0.8 μm, 30 nm silicon layer was remained as the connector of the waveguide to both the p-doped and n-doped regions after single-step dry etching, because of the etching rate difference.

2.5 References

[1] V. Kamchevska, A.K. Medhin, F. Da Ros, F. Ye, R. Asif, A.M. Fagertun, S. Ruepp, M. Berger, L. Dittmann, T. Morioka, L.K. Oxenloewe and M. Galili, "Experimental Demonstration of Multidimensional Switching Nodes for All-Optical Data Center Networks," in Proceedings of ECOC 2015, Tech. Dig. IEEE, pp. 1-3, 2015.

[2] R. Imansyah, T. Tanaka, L. Himbele, H. Jiang, and K. Hamamoto, "Mode crosstalk evaluation on optical mode switch by using MMI mode filter," IEICE Trans. Electron., vol.E99-C, no.7, pp.825–829, 2016.

[3] A. G. Medoks, "The theory of symmetric waveguide Y-junction," Radio Engineering and Electronic Physics-USSR **13**, 106 (1968).

[4] H. Sasaki and I. Anderson, "Theoretical and experimental studies on active Y-junctions in optical waveguides," IEEE J. Quantum Electron. 14, 883 (1978).

[5] M. Izutsu, Y. Nakai, and T. Sueta, "Operation mechanism of the single-waveguide Y junction," Opt. Lett. 7, 136 (1982).

[6] W. K. Burns and A. F. Milton, “Mode conversion in planar-dielectric separating waveguides,” IEEE J. Quantum Electron. QE-11, 32 (1975).

[7] R. A. Soref and B. R. Bennett, “Electrooptical effects in silicon,” IEEE J. Quantum Electron. QE-23, 123 (1987).

[8] R. Imansyah, T. Tanaka, L. Himbele, H. Jiang, and K. Hamamoto, “Electrically controlled optical-mode switch for fundamental mode and first order mode,” Jpn. J. Appl. Phys., vol.55, 8S3, 2016.

[9] S. L. Lai, D. Johnson and R. Westerman, “Aspect ratio dependent etching lag reduction in deep silicon etch,” J. Vac. Sci. Technol, 24(4), 1283 (2006).

[10] J. W. Coburn and H. F. Winters, “Conductance considerations in the reactive ion etching of high aspect ratio features,” Appl. Phys. Lett. 55(269, 2730 (1989).

Chapter 3

Mode Evaluation Method

The mode evaluation method is important to investigate the high-speed characteristic of the optical mode device because there is only one output port on the optical mode switch. Moreover, the switching is controlled by injecting the current into the phase shifter, therefore, the fundamental mode and the first mode might be mixed. Thus, the investigation of the mode crosstalk is needed. There are several techniques to distinguish the modes, by using a phase shifter [1], directional coupler [2,3], mode sorting [4], unbalanced Mach-Zehnder interferometer [5], and multimode interference (MMI) coupler [6]. Among these, we choose MMI coupler because it is easy to be integrated with the optical mode switch. There were two kinds of MMI structured that can be separated the modes; 2×2 MMI mode filter and 1×3 MMI mode filter.

Generally, the MMI devices are composed of two parts. One is the center of the multimode waveguide and the access waveguides as shown in Fig. 1. The center multimode waveguide supports a large number of modes, where the MMI occurs. A number of access waveguides are placed for the input ports and output ports. Such devices are generally referred to as N×M MMI couplers, where M and N are the numbers of input and output ports, respectively. Usually, this input and output ports are single mode waveguides for the high-performance MMI devices, however, it could be a few mode

waveguides depends on the application.

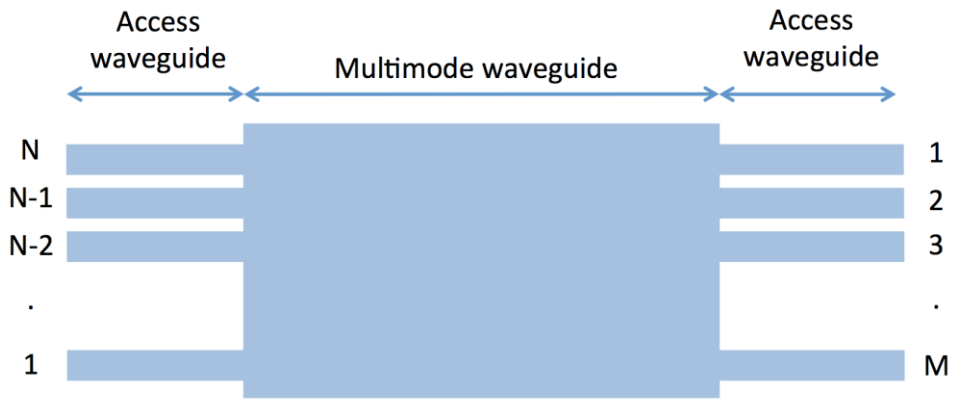

Fig. 1 N×M MMI coupler

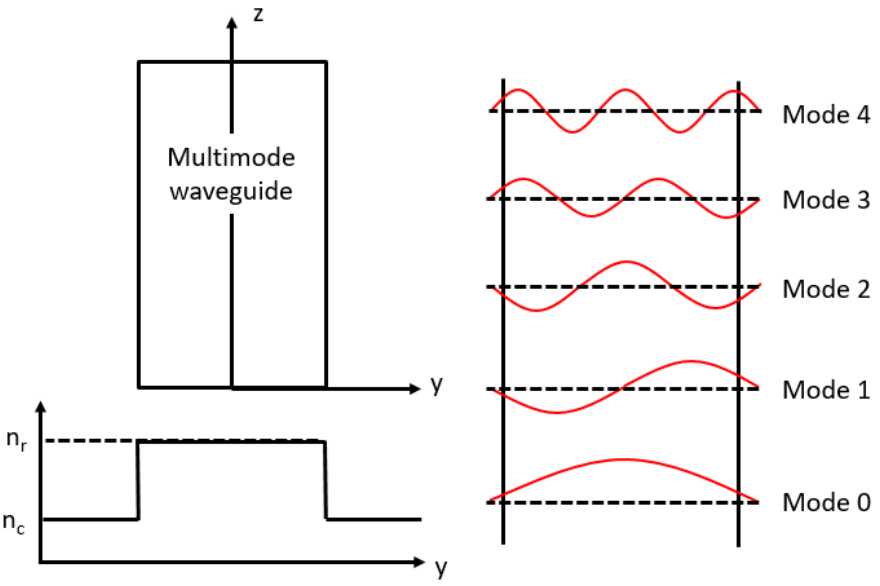

Fig. 2 Multimode waveguide, refractive index distribution and the supported modes. It shows the multimode waveguide width is W_M and the propagating direction of modes is z-direction.

The 3-D multimode waveguide can be simplified to a 2-D model by effective index method as mentioned above. Fig. 2 shows a step-index multimode waveguide with an effective refractive index n_r and a clad index of n_c. The multimode waveguide width is W_M and the propagating direction of

modes is z-direction, as shown in Fig. 2 The supported modes number can be calculated by (1a) and (1b). The electric fields distribution of these modes in the multimode waveguide is also shown in Fig. 2. From the mode power distribution, the guided modes penetrated into the cladding can be seen, which is the Goos-Hahnchen shifts.

$$u = \frac{m\pi}{2} + \frac{1}{2}tan^{-1}\left(\frac{\omega}{u}\right) + \frac{1}{2}tan^{-1}\frac{\omega_1}{u} \quad (m = 0,1,2,\dots) \tag{1a}$$

$$\phi = \frac{m\pi}{2} + \frac{1}{2}tan^{-1}\left(\frac{\omega}{u}\right) - \frac{1}{2}tan^{-1}\frac{\omega_1}{u} \quad (m = 0,1,2,\dots) \tag{1b}$$

where

$$\begin{cases} u = k\alpha \\ \omega = \xi\alpha \\ \omega_1 = \sigma\alpha \end{cases} \tag{2}$$

$$k = \sqrt{{k_0}^2{n_1}^2 - {n_1}^2} = k_0\sqrt{{n_1}^2 - {n_{\text{eff}}}^2} \tag{2a}$$

$$\sigma = \sqrt{\beta^2 - {k_0}^2{n_0}^2} = k_0\sqrt{{n_{\text{eff}}}^2 - {n_0}^2} \tag{2b}$$

$$\xi = \sqrt{\beta^2 - {k_0}^2{n_s}^2} = k_0\sqrt{{n_{\text{eff}}}^2 - {n_s}^2} \tag{2c}$$

Where n_0, n_1, and n_s is the refractive index of the coating layer, core, and cladding, respectively, and

$$tan(u + \phi) = \frac{\omega}{u} \tag{3a}$$

$$tan(u - \phi) = \frac{\omega_1}{u} \tag{3b}$$

For a symmetric waveguide, (1) can be written as

$$u = \frac{m\pi}{2} + tan^{-1}\left(\frac{\omega}{u}\right) \quad (4a)$$

$$\phi = \frac{m\pi}{2u} \quad (4b)$$

3.1 2×2 MMI mode filter

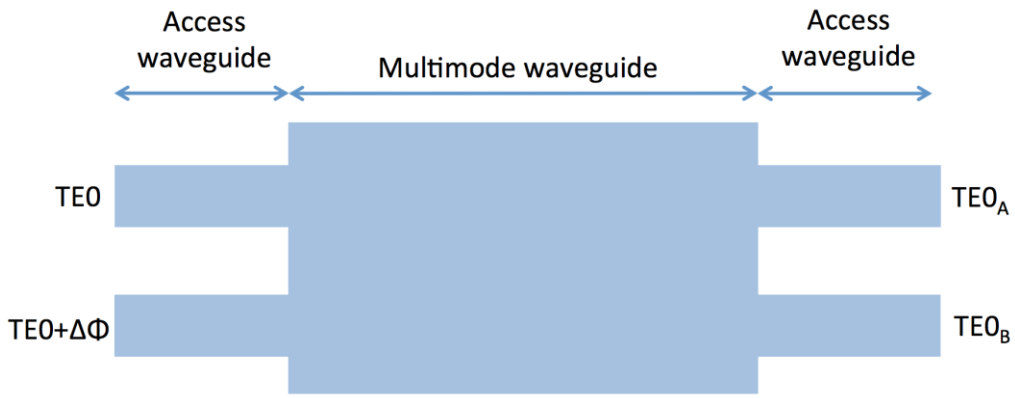

Fig. 3. The schematic of 2×2 MMI coupler. An extra Δφ is needed to make this MMI filter works. The lights will out in $TE0_A$ or $TE0_B$ depends on the Δφ of the input lights.

Fig. 3 shows the 2×2 multimode interference (MMI) coupler, there are two input ports and two output ports. This MMI coupler works as follows: when the fundamental modes get through the both of input ports with a phase difference of Δφ=π/2, TE0 input will go through the MMI structure and output from $TE0_A$ as a fundamental mode. On the other hands, when the phase difference of Δφ=3π/2, the fundamental modes get through the MMI structure and output from $TE0_B$. This state can be seen when the first-order

mode gets through the MMI because the first order mode will have a phase difference of π between the input arms.

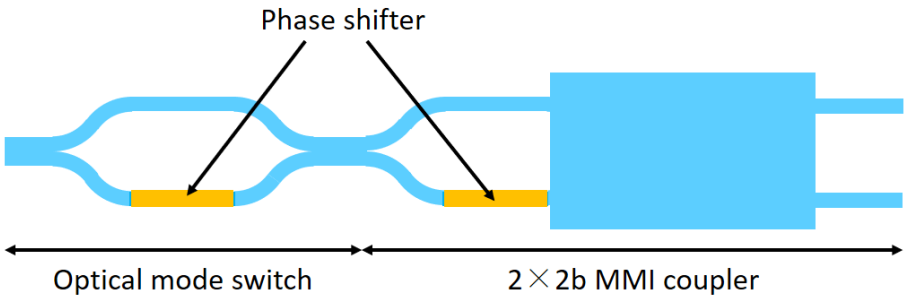

Fig. 4 The schematic of optical mode switch with 2×2 MMI mode filter. This picture shows that an extra phase shifter is neede to make the MMI mode filter works.

The merit of this MMI structure is only two output ports needed to distinguish between the fundamental mode and the first order mode. However, there are two input ports as well, thus, the output port of the mode switching needs to be divided again by Y junction and a phase change region is also needed on one of the input ports to give an extra π/2 phase difference. This structure will need a complicated fabrication process and evaluation process since another PIN junction is also needed for the MMI mode filter. Figure 4 shows the schematic mode switching with this 2×2 MMI mode filter.

3.2 1×3 MMI Mode Filter

In order to verify the potential mode crosstalk of the optical mode switch, we fabricated and integrated mode filter with the optical mode switch. This mode filter was designed based on multimode interference (MMI) coupler [7]. The principle of the MMI device is based on self-imaging as one of the properties of multimode waveguides. For filtering the fundamental mode and first-order mode, we use the simple 1×3 symmetrical rectangular shape of the MMI device that is shown in Fig. 5. The purpose is to distinguish the fundamental mode and first-order mode. It shows that, there is only 1 input port for this MMI mode filter but has 3 output ports. The merit of this MMI mode filter besides there is only one input port, a phase shifter is not needed to distinguish between the fundamental mode and the first mode. According to this merit, we chose this MMI mode filter configuration to investigate the mode crosstalk of our optical mode switch.

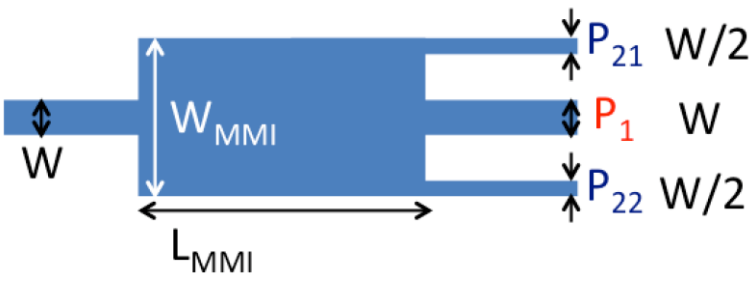

Fig. 5 The schematic of 1×3 MMI coupler. In this mode filter, only one input port is needed and no extra phase shifter is needed to make this mode filter works.

From self-imaging theory, the first-order mode injected in the center of the MMI propagates as the fundamental mode on both sides of the MMI at 3Lc/4, with Lc as beat length of the two lowest-order modes. On the other hand, the fundamental mode that is injected to the MMI at the center also propagates at the center port as the fundamental mode at 3Lc/4. Therefore, the fundamental mode propagates toward port P1 while the first-order mode will split into two and propagates toward port P21 and P22 as a single-mode. The BPM simulation result is shown in Fig. 6. Then, the transmittances of each mode are evaluated by monitoring P1, P21, and P22. The mode crosstalk was estimated by using the evaluated transmittances.

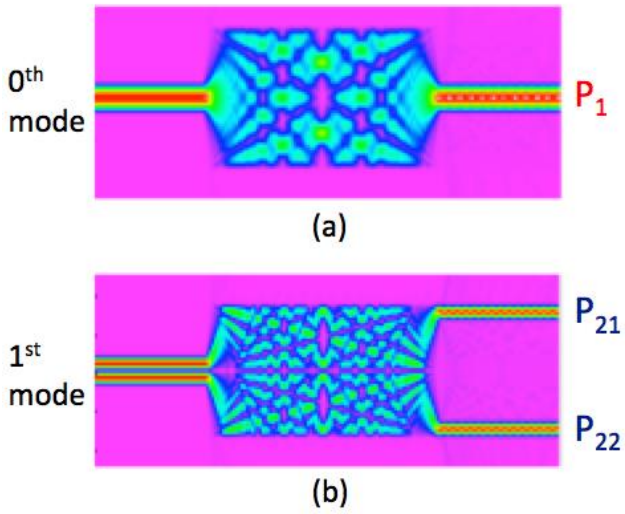

Fig. 6 BPM simulation result of Mode filter (a) Fundamental mode and (b) first order mode input. It shows that the fundamental mode will out from the center output port, while the first-order mode will out from the side output ports.

3.3 Results and discussion

In order to evaluate the 1×3 MMI mode filter, we fabricated three different L_{MMI} 208, 212, and 216 µm with the same W_{MMI} as 10 µm [8]. We fabricate these three different L_{MMI} to get the best mode crosstalk characteristic. The MMI mode filter will be fabricated and integrated with the optical mode switch, thus, the input port of the MMI mode filter should be the same as the input of optical mode switch whose width is 3 µm.

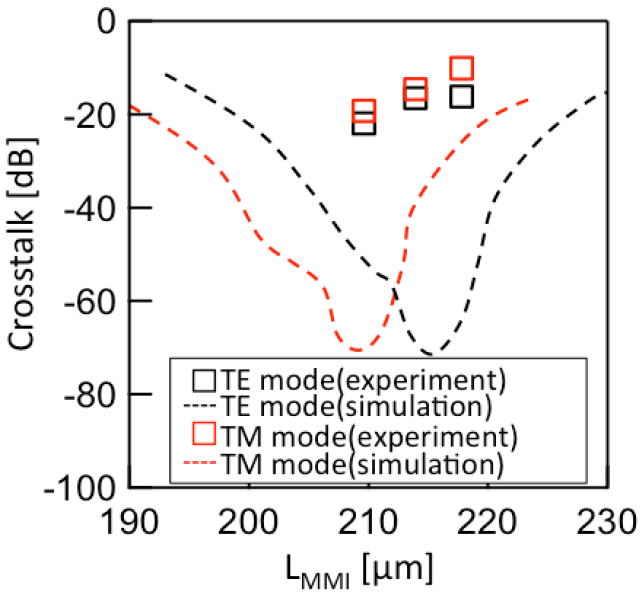

Fig. 7. Evaluated crosstalk from the fundamental mode input. It shows that the best crosstalk was got from the device with the width of 208 µm with the crosstalk of approximately -20 dB.

Figure 7 shows the result of the evaluated MMI mode filter. The dashed line shows the simulation result of this MMI mode filter as the function of L_{MMI}. The simulation shows that the TE and TM show different results which means this device has a polarization dependency. We also can see that the

best crosstalk was achieved from the L_{MMI} of 208 µm with the crosstalk of approximately -20 dB. From the result, the experimental result is totally different from the simulation result. Moreover, the experimental result looks shifted to the shorter L_{MMI} than the simulation result. This condition happened because of the fabrication error when fabricating the device. The side etching effect was not considered when designing the MMI mode filter. Side etching effect makes the W_{MMI} smaller than 10 µm. The smaller W_{MMI}, the shorter L_{MMI} needed to get a good crosstalk. Thus, the simulation result also will move to the shorter L_{MMI}. Figure 8 shows the fabricated W_{MMI}, which shows that the W_{MMI} is 0.3 µm smaller than the designed W_{MMI}.

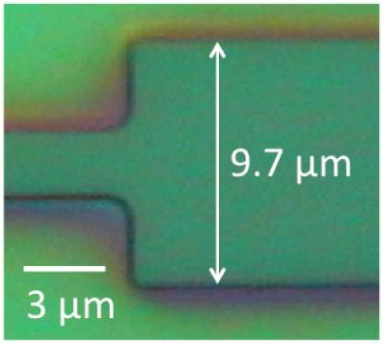

Fig. 8 The fabricated MMI mode filter. It shows the fabrication error of the mode filter, a side etching of 0.3 µm was investigated.

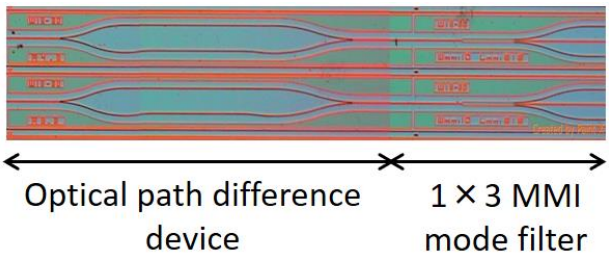

Fig. 9. Shematic of the integrated optical path difference device and 1×3 MMI mode filter.

For comparison purpose, we also fabricated different length variation for the path different device. The length difference is 0 µm, 0.22 µm, 0.26 µm and 0.30 µm that correspond to the refractive index change ΔN of 0, 0.003, 0.004, and 0.005, respectively. We integrated the path difference device with the MMI mode filter to investigate the characteristic of MMI mode filter when the first-order mode is input into the MMI mode filter. Figure 9 shows the schematic of the integrated optical path difference device and the MMI mode filter.

As shown as a solid line in Fig. 10, the cross-state is realized at ΔN = 0.004. This result is matched well with the theoretical results shown as dashed lines in the same figure. The estimated crosstalk was approximately -10 dB for both TE and TM modes at exactly same ΔN. This value is not sufficient for the practical use, however, there is a possibility that the best point may exist at slightly different ΔN of bellow 0.004.

From the Fig. 10, it shows the insertion loss of this device which is approximately 20 dB with the crosstalk of approximately -10 dB. This insertion loss is the collective loss from the coupling loss, loss from the path difference device, and also fr om the MMI mode filter. This condition can be improved by applying the taper into the MMI mode filter as shown in Fig. 11. By the application of such a taper, the MMI coupler performance will be increased [9, 10].

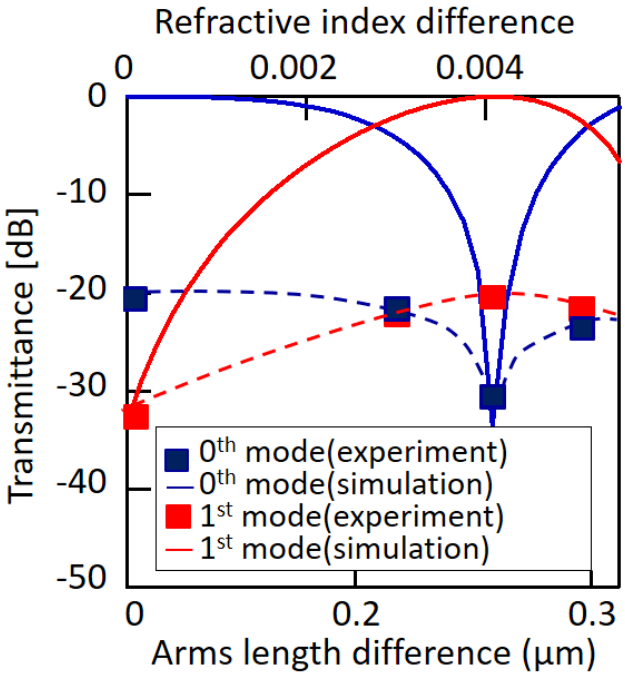

Fig. 10. The Evaluated transmittance as a function of ΔN for TE mode. The dashed line shows the experiment results from the arm's length different of 0 μm, 0.22 μm, 0.26 μm, and 0.3 μm, while the solid lines shows the simulation results..

The taper is an essential approach to diminish the transition loss between these two dissimilar waveguides of the access waveguide and the multimode waveguide. This dissimilarity makes the modes that propagate inside the MMI changes the phase, thus in some certain length of L inside the MMI differs by 2m, where is m is integer [11]. As the taper width W_t getting closer to the MMI width, then the transition of the access waveguide and the MMI will be smaller. Without taper, the field along the the MMI section diffracts dramatically first and then converges at some L.

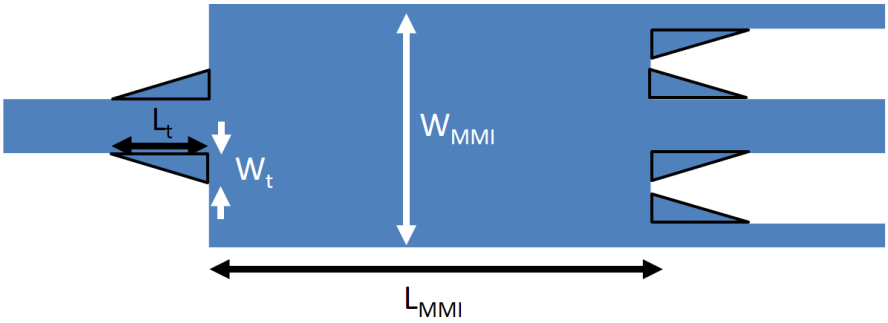

Fig. 11. 1×3 MMI mode filter with taper. The taper will make the transition of the access waveguide and the MMI smaller.

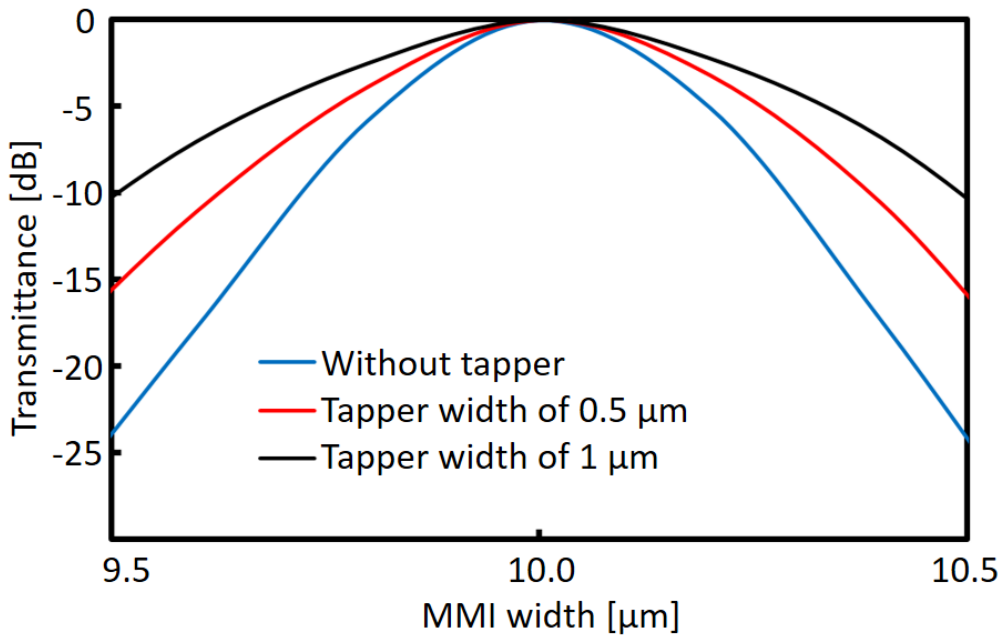

Fig. 12. Transmittance simulation of fundamental mode input in 1×3 MMI mode filter with tapper. An improvement of 10 dB at a fabrication error of 0.5 µm can be gotten by using a tapper with the width of 1 µm.

Figure 12 shows the transmittance simulation for the MMI mode filter with the application of the tapers. It shows the transmittance as a function of MMI width while the MMI length was fixed. The blue line shows that the

transmittance of the fundamental mode when there is no taper in the 1×3 MMI mode filter. The figure also shows that the MMI mode filter error without taper could reach 25 dB/0.5 μm. As already mentioned that the fabrication error of the MMI mode filter was 0.3 μm, the propagation loss from the MMI mode filter itself could reach approximately 15 dB. On the other hand, the application of the taper can improve the MMI mode filter error into only -15 dB/0.5 μm for the width taper of 0.5 μm and -10 dB/0.5 μm for the taper width of 1 μm.

3.4 Conclusions

In this chapter, we first gave a brief explanation of the mode evaluation method that we are using for the MMI mode filter. We were using the 1×3 MMI mode filter because there is only one input port for this MMI mode filter and no phase shifter is needed to make the MMI mode filter working. As a result, MMI mode filter with W_{MMI} of 10 μm and L_{MMI} of 208 μm shows the best mode crosstalk results. By integrating the MMI mode filter, a path difference device was integrated with the MMI mode filter to see the MMI mode filter performance over mode switching device. The result shows that the insertion loss of this device is approximately -20 dB with the crosstalk of approximately -10 dB. This MMI mode filter performance can be increased by applying the taper in the MMI coupler. Simulation result shows that the MMI mode filter with the taper width of 1 μm shows the best result of fabrication tolerance with only -10 dB/0.5 μm.

3.5 References

[1] E. Ip, M. Li, K. Bennet, Y. Huang, A. Tanaka, A. Korolev, K. Koreshkov, W. Wood, E. Mateo, J. Hu and Y. Yano, "146 λ ×6×19-Gbaud Wavelength- and Mode-Division Multiplexed Transmission over 10×50-km Spans of Few-Mode Fiber with a Gain-Equalized Few-Mode EDFA," Tech. Dig. OFC, PDP5A.2, 2013

[2] Y. Ding, J. Xu, F. D. Ros, B. Huang, H. Ou and C. Peuchret, "On-chip two-mode division multiplexing using tapered directional coupler-based mode multiplexer and demultiplexer," Opt. Express, vol. 21, No. 8, pp. 10376-10382, 2014.

[3] T. Uematsu, K. Saitoh, N. Hanzawa, T. Sakamoto, T. Matsui, K. Tsujikawa and M. Koshiba, "Low-loss and broadband PLC-type mode (de)multiplexer for mode-division multiplexing transmission," Tech. Dig. OFC, OTh1B.5, 2013.

[4] S. Martínez-Garaot, S. Tseng and J. G. Muga, "Compact and high conversion efficiency mode-sorting asymmetric Y junction using shortcuts to adiabaticity," Opt. Letters, vol. 39, No. 8, pp. 2306-2309, 2014.

[5] W. Y. Chan and H. P. Chan, "Reconfigurable two-mode mux/demux device," Opt. Express, vol. 22, No. 8, pp. 9282-9290, 2014.

[6] J. Leuthold, R. Hess, J. Eckner, P. A. Besse and H. Melchior, "Spatial mode filters realized with multimode interference couplers," Opt. Letters, vol. 21, No. 11, pp. 836-838, 1996.

[7] H. V. Demir, V. A. Sabnis, O. Fidaner, S. Latif, J. S. Harris, and D. A. B. Miller. “Novel optically-controlled optical switch based on intimate integration of surface-normal photodiode and waveguide electroabsorption modulator for wavelength conversion” LEOS [Tucson, Arizona. 2003]

[8] R. Imansyah, T. Tanaka, L. Himbele, H. Jiang, and K. Hamamoto, “Mode crosstalk evaluation on optical mode switch by using MMI mode filter,” IEICE Trans. Electron., vol.E99-C, no.7, pp.825–829, 2016.

[9] D. S. Levy, R. Scarmozzino, Y. M. Li, and R. M. Osgood, “A new design for ultracompact multimode interference-based 2×2 couplers,” IEEE Photon. Technol. Lett., vol. 10, pp. 96–98, 1998.

[10] L. Spiekman, Y. Oei, E. Metaal, F. Groen, I. Moerman, and M. Smit, “Extremely small multimode interference couplers and ultrashort bends on InP by deep etching,” IEEE Photon. Technol. Lett., vol. 6, pp. 1008–1010, 1994.

[11] C. H. Chiu and C. H. Chen, “Taper-integrated multimode-interference based crossing for silicon wire waveguides,” Proc. of SPIE., vol. 7606, 76061C, 2010.

Chapter 4

Mode-Switching Time of 2×2 Optical Mode Switch

Optical mode switch works by injecting the current into the p-i-n phase shifter. As already mention in section 2.2.2, intrinsic silicon (i-Si) is essential to keep the propagation loss low. There are two important things in the phase shifter that will determine the performance of the optical mode switch such as the power needed to change the phase and the switching time characteristic. This phase shifter performance characteristic is determined by the shape and the ion implantation to form the p-i-n junction.

4.1 P-I-N trench fabrication process.

As mentioned in section 2.2.2, the phase shifter was realized by fabricating a trench p-i-n junction structure to simplify the fabrication process. Due to the limitation of the specification of the lithography process, the narrowest pattern of the common photolithography stage aligner is 1 μm. Thus, the patterning for the device was outsourced from 3D semiconductor research center.

Figure 1 shows the fabrication flow of the optical mode switch before the implantation of Boron. First, after the waveguide was formed, the SiO_2 was deposited using plasma CVD that was outsourced to Semiconductor Center in Kitakyushu, as shown in Fig. 1 (a). This SiO_2 layer is needed in order

to protect the waveguide from the ion implantation process. Next, the photoresist was deposited on the top of the SiO_2. In order to open the window of SiO_2 on one side of the ion implantation area for Boron ion implantation, the photoresist was patterned using stage aligner and developed. This process is shown in Fig. 1 (c) to Fig. 1 (d). The SiO_2 was etched chemically using BHF, as shown in Fig. 1 (e). Then Boron ion was implanted to form the P-type Si in one depositing area for the phase shifter, as shown in Fig. 1 (f).

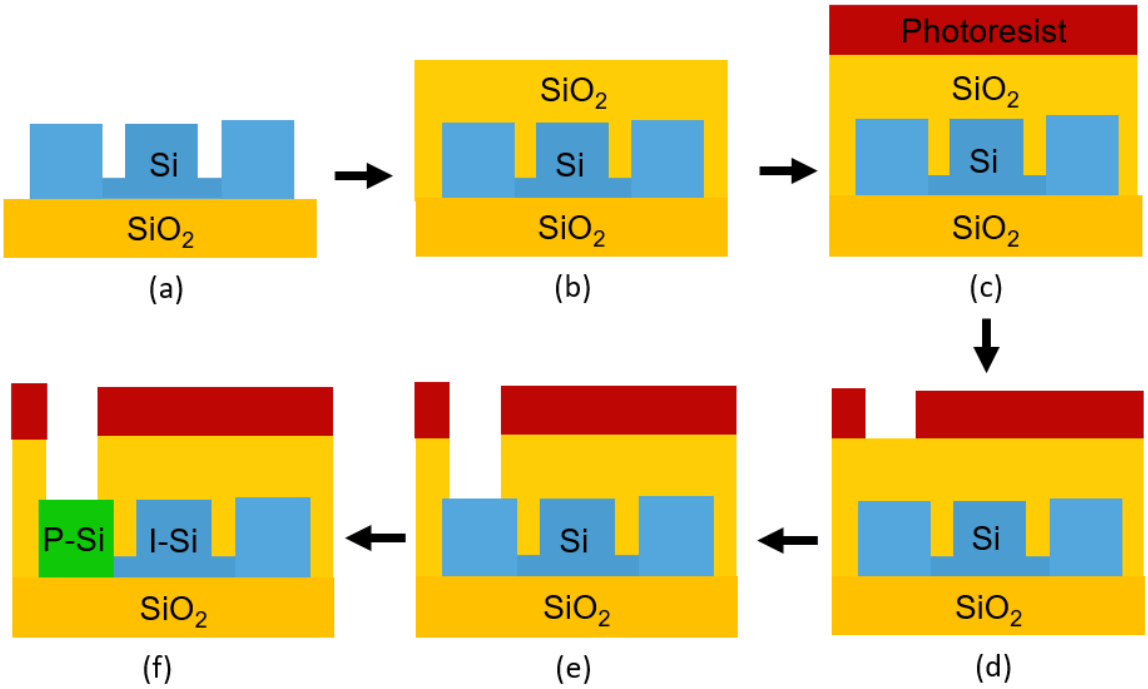

Fig. 1. Fabrication flow of Boron ion implantation from the cross section or the phase shifter; (a) p-i-n trench structure, (b) SiO_2 deposition, (c) Photoresist deposition, (d) Photoresist patterning and developing, (e) SiO_2 etching, and (f) Boron ion implantation.

Figure 2 shows the fabrication flow of the Phosphorus ion implantation. After Boron ion implantation was finished, the photoresist was removed using plasma ashing and chemical removing. After that, the photoresist was deposited one more time to implant the Phosphorus ion, as shown in Fig. 2 (a). Then, the photoresist was patterned and developed to open the other side window of SiO_2 for phosphorus ion implantation, as shown in Fig. 2 (b). Next, the SiO_2 layer was etched using BHF to open the window for Phosphorus ion implantation, as shown in Fig. 2 (c). Next, the Phosphorus ion was implanted into the wafer to form the N-type Si, as shown in Fig. 2 (d). Then, at last, the photoresist was removed using a plasma ashing process and chemical removing.

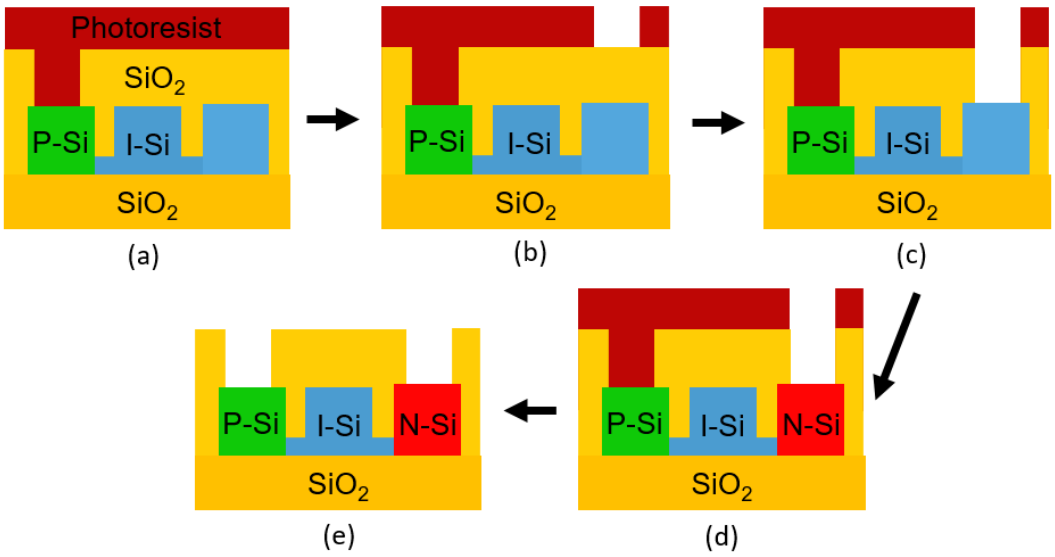

Fig. 2. Fabrication flow of Phosphorus ion implantation from the cross section or the phase shifter; (a) Photoresist deposition, (b) Photoresist patterning and developing, (c) SiO_2 etching, (d) Phosphorus ion implantation, and (e) Photoresist removing.

4.2 Ion implantation distribution

The ion implantation and distribution is important because it will determine the capacitance of the p-i-n junction. The capacitance of the p-i-n junction is dependent to the depletion region which is affected by the distribution of the ion inside the p-i-n junction. The switching speed will be increased if the capacitance of the p-i-n junction higher.

Ion implantation is done by implanted the dopant ions into the semiconductor by high energy ion beams. However, the distribution of the ion inside the semiconductor will not be uniformly distributed. The distribution will make a Gaussian distribution where the dose will reach the peak in some certain position inside the semiconductor. The profile of distribution is determined by the ion element and energy. The ion distribution was simulated using a software called “Stopping and Range of Ions in Matter” (SRIM) [1]. Fig 3 shows the implantation direction of the ion, the ion beam comes from above the device, thus the ion will be implanted from the surface of the device.

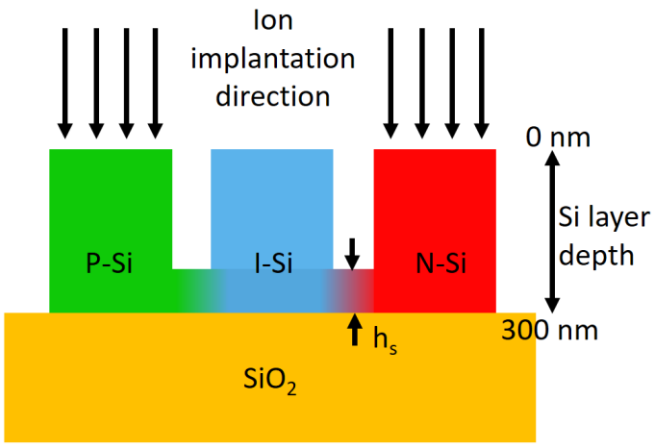

Fig. 3. Ion implantation direction looked from the cross section of the phase shifter . The ion is implanted from the surface of the device, it is then distributed inside the Si layer.

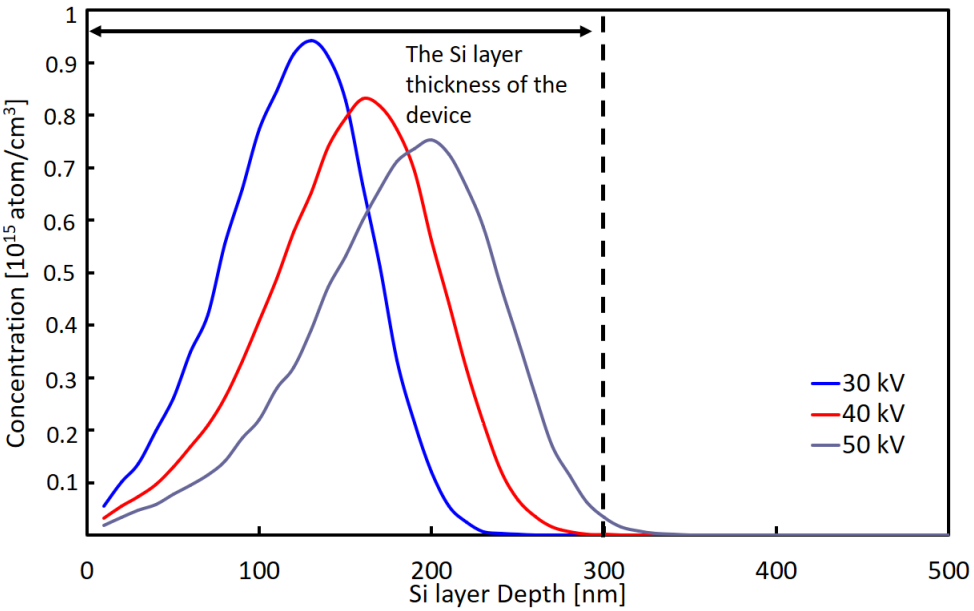

Fig. 4. Boron ions distribution inside the Si. It shows that the peak of the distribution of Boron atom is located in the center of the Si layer of 300 nm when the ion implantation voltage is 30 kV.

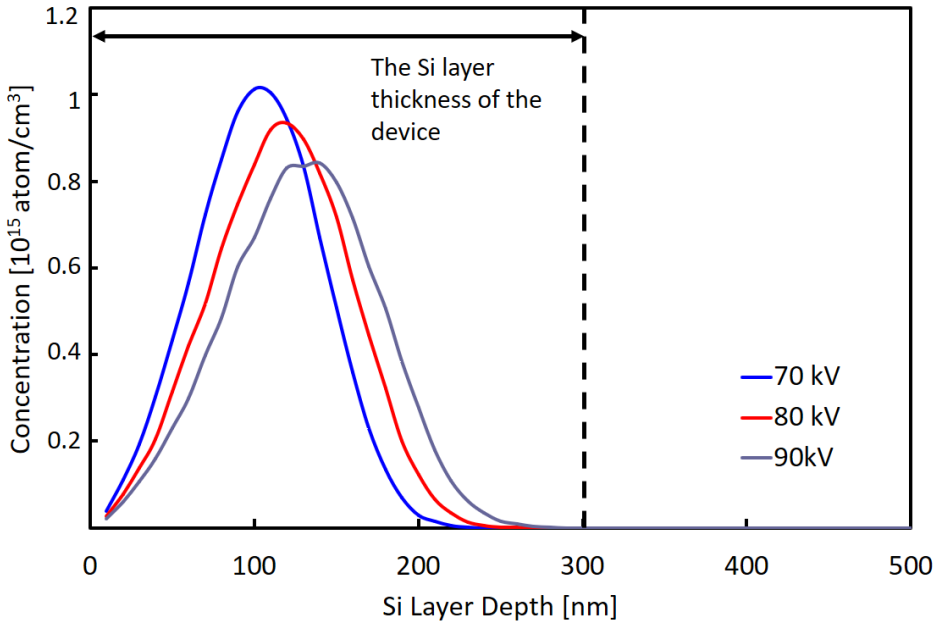

Fig. 5. Phosphorus ions distribution inside the Si. Differently from Boron, Phosphorus ions need more energy to penetrate inside the Si layer, 90 kV of ion implantation voltage is needed to make the ions distributed in the middle of Si layer of 300 nm.

Figure 4 shows the ion distribution of Boron inside the semiconductor for difference energy. The Si depth was set up as 1000 nm while the energy ion beams were 30 kV, 40 kV, and 50 kV. The higher energy ion beams, the deeper peak of ion distribution inside the semiconductor, however, the peak concentration is lower. Figure 5 shows the Phosphorus ions distribution inside the Si. From the figures 4 and 5, the higher implantation energy is needed to implant the phosphorus ion inside the Si. This condition has occurred because the phosphorus atom is much larger and heavier than the boron atom.

4.3 Atoms diffusion in Si

In order to control the ion distribution inside the Si, diffusion is needed. Diffusion can be done by an annealing process. The diffusion property can be described and solved by a diffusion function [2]. The diffusion function is explained as below:

$$\mathrm{J} = -\mathrm{D}\frac{\partial C_V}{\partial x} \qquad (1)$$

J is the number of dopant atoms passing through an area in a unit time, while C_V is the dopant concentration per unit volume. D is the diffusion coefficient of diffusivity with a unit of cm^2/s and x is the distance along the diffusion path. By considering J and C are the functions of distance x and time t, the equation (1) can be written as:

$$\mathrm{J(x,t)} = -\mathrm{D}\frac{\partial C_V(x,t)}{\partial x} \qquad (2)$$

We assumed that no material is formed or consumed in the host semiconductor, we then obtain:

$$\frac{\partial C_V}{\partial t} = -\frac{\partial J}{\partial x} = \frac{\partial}{\partial x}\left(D\frac{\partial C_V}{\partial x}\right) \qquad (3)$$

When the concentration of the dopant atoms is low, the diffusion coefficient can be considered independent of the doping concentration:

$$\frac{\partial C_V(x,t)}{\partial t} = D\frac{\partial^2 C_V(x,t)}{\partial x^2} \qquad (4)$$

To solve this function, ion concentrations, boundary, and initial condition is needed. The boundary condition is described as follow:

$$\int_0^\infty C_V(x,t) = A \tag{5}$$

Which means that the dopant atoms (A) is constant. While the dopant concentration at x=∞ is determined as:

$$\mathrm{C}_V(x=\infty,t) = 0 \tag{6}$$

If the peak of dopant atoms concentration is located outside the surface (x=0) when t=0, the initial condition is expressed as:

$$\mathrm{C}_V(x,t=0) = 0 \tag{7}$$

Thus, the diffusion condition is expressed by Gaussian profile:

$$C_V(x,t) = \frac{A}{\sqrt{\pi D t}} \exp\left(-2\left(\frac{x}{4\sqrt{Dt}}\right)^2\right) \tag{8}$$

With the assumption of the peak position of initial dopant distribution is not located in the surface but in the position of x=R_p. Thus the diffusion equation become:

$$C_V(x,t) = \frac{\Phi}{\sqrt{\Delta R_p^2 + 2D_c t}\,\sqrt{2\pi}} \exp\left(-\frac{(x-R_p)^2}{2(\Delta R_p^2 + 2D_c t)}\right) \tag{9}$$

Here, x is the depth of the semiconductor, Rp is the peak depth of dopant, t is annealing time, D_c is the dispersion constant, and Φ is implantation dose [3].

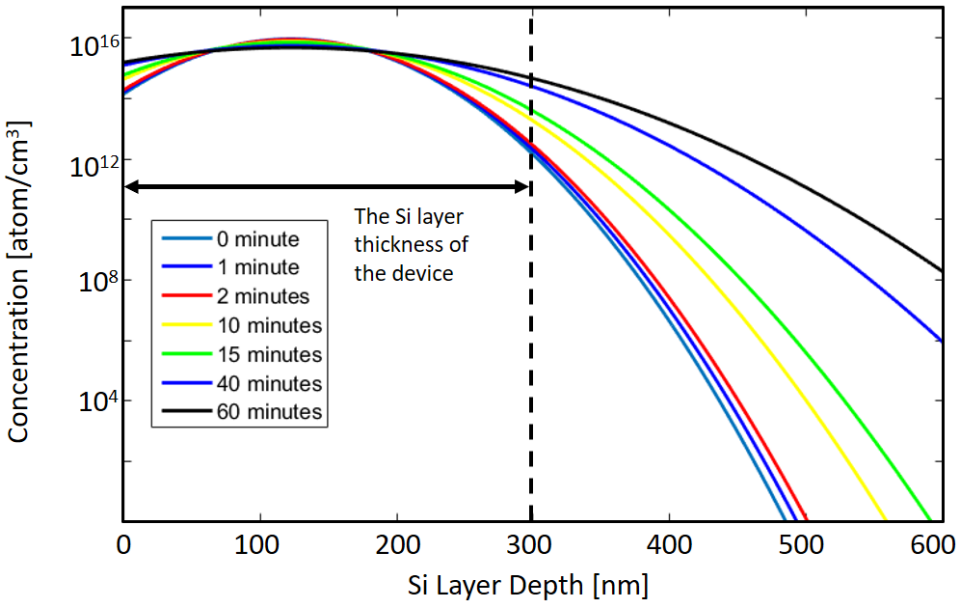

Fig. 6. Dispersion of Boron as a function of time. It shows that the boron ions are distributed uniformly in 300 nm layer of Si after 60 mins thermal annealing.

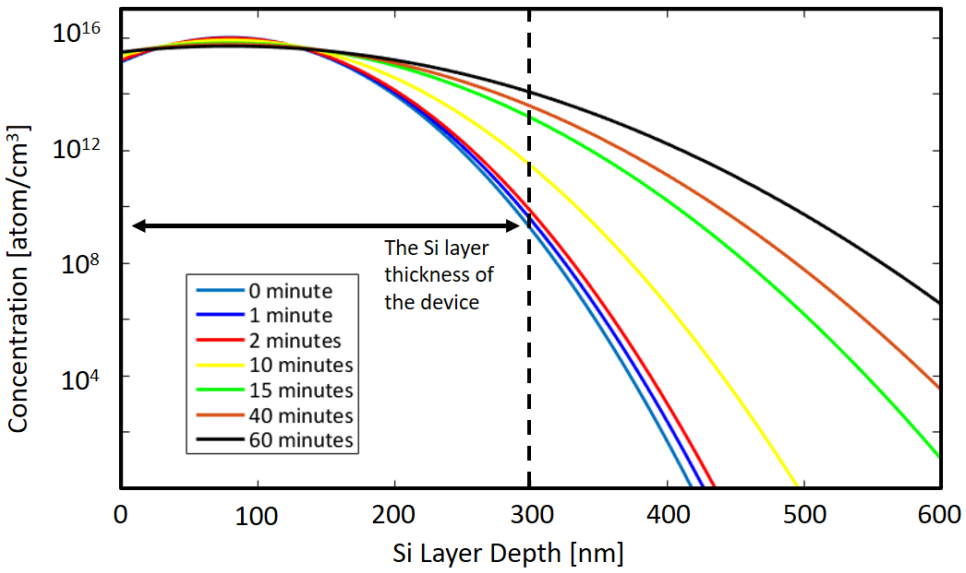

Figure 7. Dispersion of Phosphorus as a function of time. Almost the same with boron ions, phosphorus ions are distributed uniformly in 300 nm layer of Si after 60 mins thermal annealing.

Figure 6 and Figure 7 show the atoms dispersion simulation in a function of time for Boron and Phosphorus, respectively. As shown in the figure, the annealing time makes the distribution of the atoms dispersed both into the surface and deep down to the Si wafer. This distribution is not only to the vertical direction of the wafer but also into the horizontal direction of the Si wafer which is needed to make the Boron ion penetrate closer to the intrinsic Si (I-Si) to fill the gap between the doped region and the I-Si waveguide as shown in the Fig.8. The gap length was 800 nm, thus the annealing time of 60 minutes should be enough to fill the gap area with some of the Boron atoms. If the ion fills the gap area, the intrinsic area will be narrower and the resistance will be smaller, thus, the switching time also will be faster.

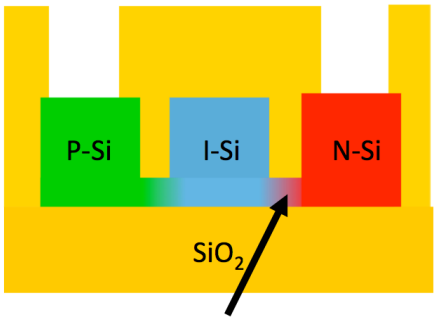

Fig. 8. Dispersion of Phosphorus as a function of time. Some of the boron ions and phosphorus ions is needed to be distributed into the gap region between the I-Si and the doped region.

4.4 Results and discussion

We fabricated two open spaces (W_t) to realize these p-i-n structures, the narrow (0.8 μm) and wide (30 μm) open spaces. The remaining Si layer of 30 nm from the original 260 nm Si thickness of the SOI wafer realized in the 0.8 μm narrow open space. Meanwhile, the entire Si layer is completely etched in the wide open space. For the ion implantation, the p-doped and n-doped regions are implanted with a dosage of 2×10^{15} ions/cm^2, and the ion beam energies were 120 keV and 45 keV, respectively. The annealing process for both ion implantation was done at 1000^{o}C for 30 minutes. By using this structure and ion implantation dosage, the refractive index change region based on p-i-n junction is realized to make a phase difference between the arms. Then, Ti and Al layers are coated on the top of doped regions for current injection.

In order to confirm the mode switching operation, we injected fundamental mode of 1550 nm laser to the input port of the implemented device and injected the electric current to the phase shift region of the implemented device. By subtracting the insertion loss of the implemented device, Fig. 9 shows measured normalized transmittance of the two-mode switch at the wavelength of 1550 nm as a function of the injected current for TE mode.

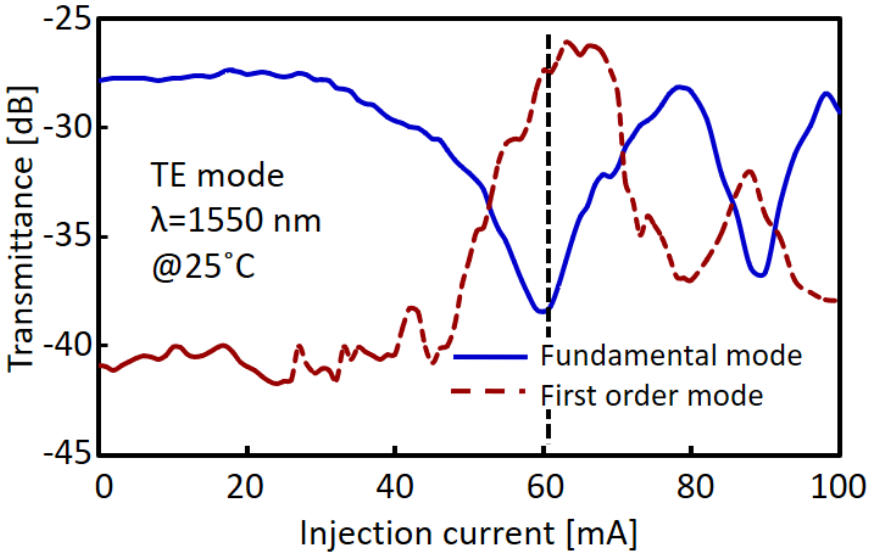

Fig. 9. Measured normalized transmittance as a function of the injected current. It shows that the injection current of 60 mA is needed to switch the modes.

The measurement was done by using the MMI mode filter. Blue (solid) and red (dash) lines show the transmittances of the fundamental mode and the first order mode respectively. The insertion loss of the device was 27 dB. As determined by comparing with the loss analysis of a straight waveguide fabricated simultaneously on the same wafer, there was no significant radiation loss at the Y-junction and the trench region. The main cause of the high insertion loss is fiber-coupling loss and propagation loss [4]. As mentioned in Chapter 3, the insertion loss for the path difference device is also approximately 20 dB with the most of the propagation loss came from the fabrication error from the MMI mode filter.

When injecting current, both of the power changed dramatically where the dip of fundamental mode was at 58 mA while the peak of first-order mode was at 62 mA, showing that the switching state occurred at approximately 60

mA (5.7 V). The resistance of the device was 100 Ω from the measurement by using IV meter. The maximum power of the first-order mode is higher than that of the fundamental mode. This condition occurs because we only measured one of the side output ports in the MMI mode filter and assumed that the output power from both of the side output ports to be the same. However, owing to the imperfection of the fabrication process, especially in the dimensions of the MMI mode filter, the output power of the side output ports is slightly different where the switching current and voltage were found to be relatively high. However, these will be improved by the optimization of the non-doped region, as it was approximately 5 µm.

The mode crosstalk is measured to be −10 dB. This experimental result of mode crosstalk is higher than the simulation result [5], mainly because of the dimension inaccuracies of the fabricated device due to fabrication errors. The actual width of the fabricated MMI mode filter shows a difference of 0.3 µm compared to the designed value, as discussed in Chapter 3. If this error can be decreased less than 0.1 µm, a lower mode crosstalk of −40 dB is expected. The switching behavior for the TE and TM modes should be different because the effective refractive index in a flat core Si waveguide generally have a strong polarization dependence [6].

We also confirmed the device output field at different driving current captured with an infrared camera. Figure 10 shows the results for the input light of the fundamental mode. At 0 mA, the image shows a clean fundamental mode pattern as shown in Fig. 10 (a). When current increases to 62 mA, the

image shows a clean first order mode as shown in Fig. 10 (b). Since the device output field shows clear fundamental mode and first-order mode patterns under different current, the phase error in the MZI arms due to fabrication error does not influence the mode switching operation.

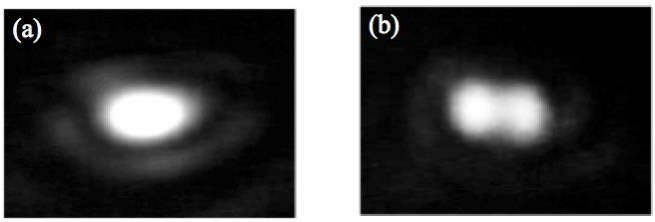

Fig. 10. Output near-field images captured by an infrared camera at different driving current, (a) 0 mA and (b) 62 mA.

To measure the optical mode-switch dynamic response, we injected the electrical pulse-pattern signals to the phase shift region of the implemented device. A CW fundamental mode light of 1550 nm was injected, and the output light signal was monitored with a digital sampling oscilloscope using lensed fiber [7]. The insertion loss of the implemented device was compensated by using erbium-doped fiber-amplifiers (EDFA).

Figure 11 (a) shows the device output status from the injection signal of a 1500 ns with 2 V peak-to-peak square pulse (Fig. 11 (b)). Because the working voltage of the device was 5.7 V, to get a significant difference of fundamental mode when the current is injected and not injected, the signal was set to be between 3 V and 5 V by adding the bias DC as 3V. From this condition, the status was evaluated by monitoring the output power at the fundamental mode port of the MMI filter under the room temperature of

25˚C. When the current is set to cross-state (approx.60 mA, 5 V), the device status shows a lower optical power level which corresponds to the first order mode. In the case that the current is set to bar-state (3 V), the device status shows a higher optical power level, which corresponds to the fundamental order mode.

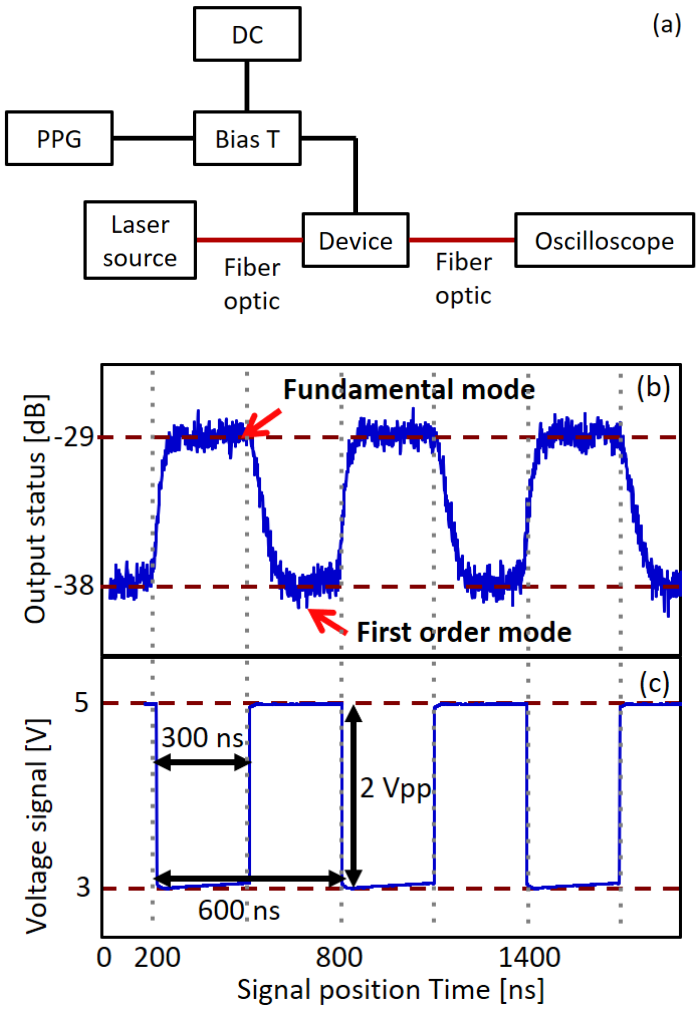

Fig. 11. Experiment's configuration set up and the dynamic mode-switching results. (a) Experiment's configuration set up, (b) device output status, and (b) voltage signal. The signal was given to the device by using bias T with the Vpp of 2 V, bias DC of 3 V was used to get a clear status of fundamental mode and the first order mode.

We filtered the noise signal from the results by using Fast Fourier transform filters. The evaluation signal showed 10–90% transit time as the switching time. Figure 12 shows the results after noise filtering. The switching time of 40 ns for the first-order mode to fundamental mode and a switching time of 60 ns for the fundamental mode to first order mode was observed as shown in Fig. 11.

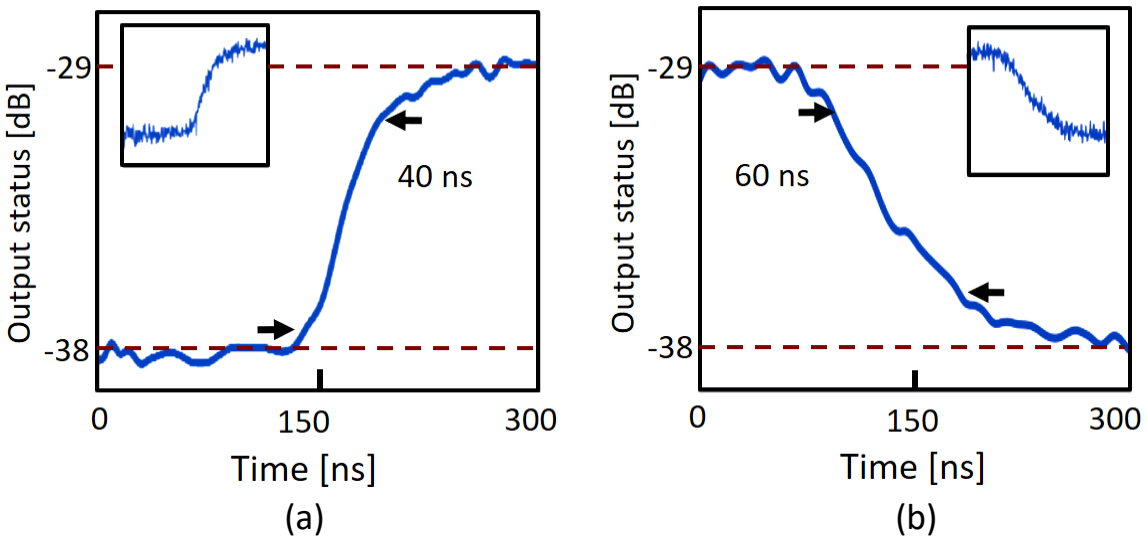

Fig. 12. Measured mode-switching time result after filtering noise. (a) First order mode to fundamental mode, and (b) fundamental mode to first order mode.

From the graph above, the frequency response can be investigated by measure the output spectrum of the device to the input signal. Because the detected output signal was the fundamental mode that was detected when the injected current was zero or the input signal was “off”. To compare the input signal and output signal, the input signal needed to be converted into a reverse signal.

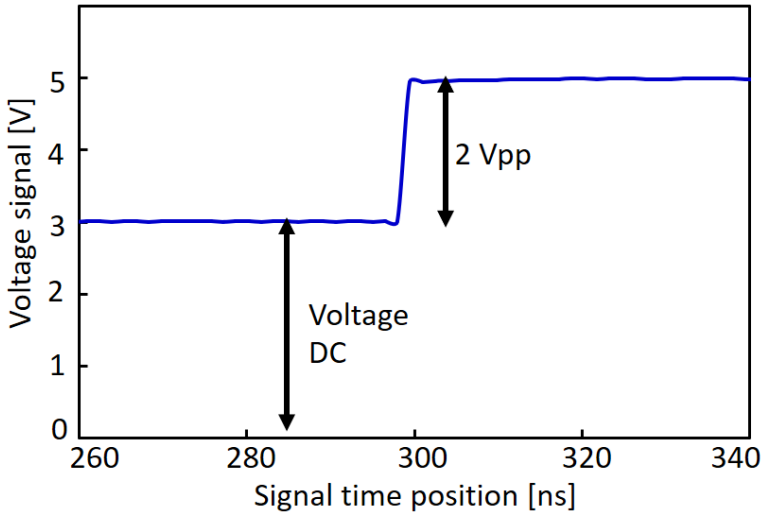

Fig. 14. The reverse signal of the input signal. The x axis shows the signal time position, the signal switch from off to on condition at 300 ns for one signal from 0 to 600 ns.

Figure 14 shows the reverse signal of the input signal in order to get the frequency response. The “off” condition now represents when the current was injected into the device, while the “on” condition represents when the current was not injected into the device. The current was injected with the 2 Vpp (21.053 mA/Vpp). It looks like between the “off” and “on” condition is not vertically changed, there is a slope with the distance of 1 ns. Fig. 15 shows the slope in the transition of “off” and “on” condition.

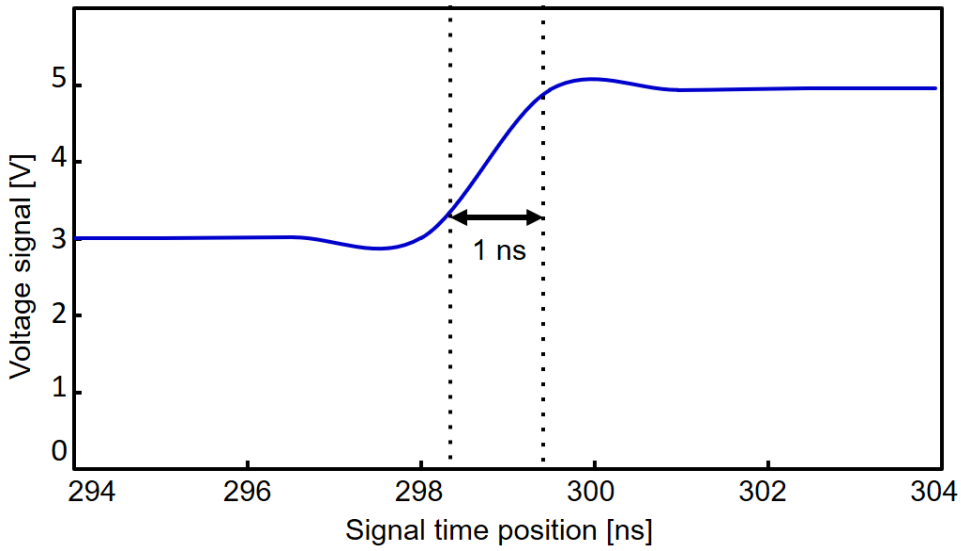

Fig. 15. The slope in the transition between the “off” and “on” condition of input signal. The x axis shows the signal time position for the range of 10 ns in the switching part. It shows that the signal switches from “off” to “on” in 1 ns.

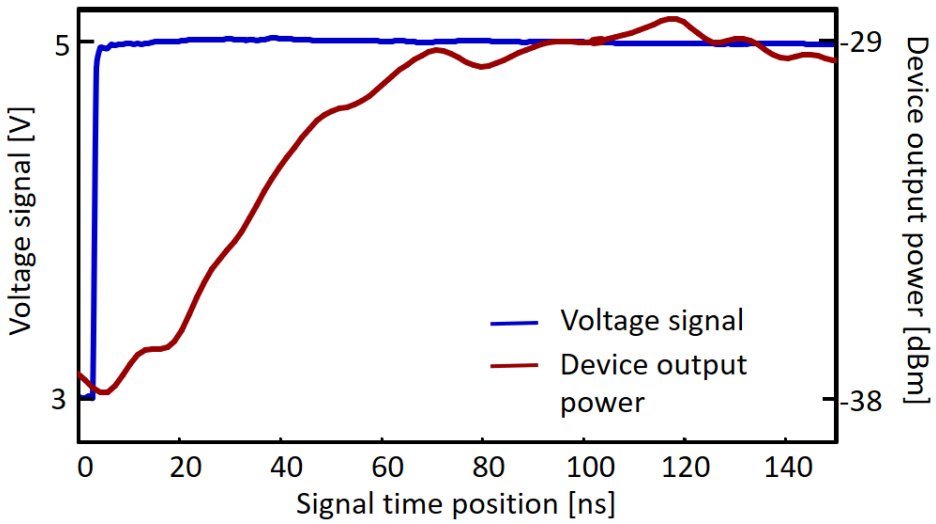

Fig. 16. The comparison between input signal and the device response. The x axis shows the time start from the signal switches form “off” to “on”.

In order to get the frequency response, the comparison between the input signal and the device response is needed. Fig. 16 shows the comparison between them. In the figure, it shows that the device has the lowest response in the high frequency (approximately in order of 1 ns) while it shows the high response for the low frequency of less than 3 dB (approximately at the point of 60 ns). The detail of the frequency response is explained in Fig. 17.

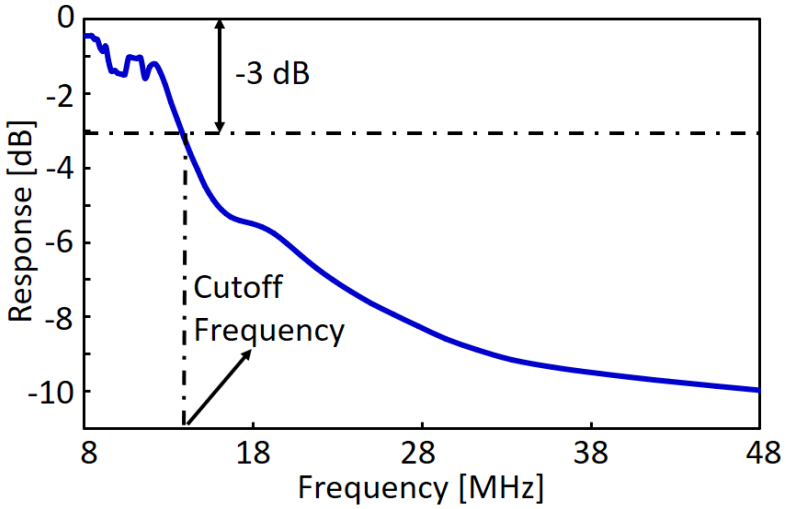

Fig. 17. Frequency response of the 2×2 Optical Mode Switch. It shows the cut-off frequency of the device of 14 MHz.

Figure 17 shows the Frequency response of the 2×2 Optical Mode Switch. The result shows the frequency response of the 2×2 Optical Mode Switch to be nearly flat for low frequencies and all the input signal is passed directly to the output, resulting in a gain until it reaches its cut-off frequency point at 14 MHz. The cut-off frequency or -3 dB point, can be found using the standard formula,

$$f_c = \frac{1}{2\pi RC} \qquad (10)$$

With the cutoff frequency f_c of 14 MHz, the RC of 2×2 Optical Mode Switch is 11.3 ns. With the measured Resistance (R) of the device by using forward bias IV characteristic was 100 Ω, however, this resistance is different in a high frequency. At higher frequencies, the number of free carrier charges stored in the intrinsic does not appreciably change within the short period of the signal, and they constitute a conductive gas or plasma. The PIN diode behaves as a current controlled resistance whose value can be expressed as,

$$R_f = \frac{W^2}{2\mu\tau I_F} \tag{11}$$

Where μ is the mobility of carriers in the intrinsic region, W is the I-region width, τ is the carrier lifetime and I_F is the forward bias current. That shows that the high frequency resistance is smaller than the corresponding low frequency resistance at the same bias current [11]. Thus, the resistance of the device is expected as lower than 100 Ω, then the Capacitance (C) of the optical mode switch device is higher than 113.68 pF.

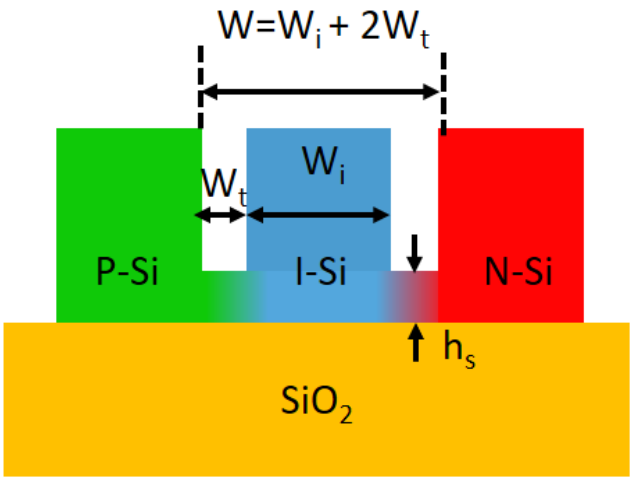

Fig. 18. Schematic cross-section of p-i-n trench structure after implantation of p-doped and n-doped.

To improve switching performance of the optical mode switch, the geometric parameters should be optimized for the p-i-n structure. One parameter is h_s, as shown in Fig. 18. The RC time constant does not depend on h_s because of the h_s of the resistance and the junction capacitance will cancel each other. On the other hand, a smaller h_s is beneficial in decreasing radiation loss, as discussed in Chapter 2. However, a certain thickness is needed for the remaining Si layer to carry current between p/n regions and the waveguide. Therefore, the h_s of 30 nm was set in this study, under which the optical loss is negligible even with a small W_t.

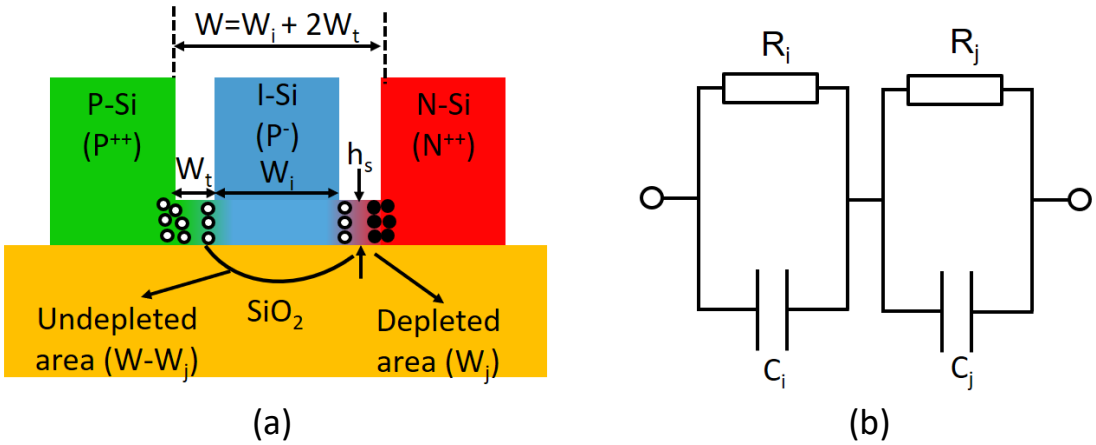

Fig. 19. Configuration of (a) p-i-n junction with depleted area (W_j) and undepleted area (W_i) and (b) equivalent circuit of p-i-n junction.

Since the I-Si is actually not a pure Si but a low concentration of Boron-doped Si, the equivalent circuit of p-i-n diode can be drawn as Fig. 19 because there are 2 main regions, depleted and undepleted [12]. Each of them is represented by R and C elements with subscript j and I corresponding to the depleted and undepleted region. The capacitances of the two base regions are:

$$C_j = \frac{\varepsilon\varepsilon_0 S}{W_j};\ C_i = \frac{\varepsilon\varepsilon_0 S}{W - W_j} \quad (12)$$

Where S is the cross section area, W is the diode base width. The depletion layer width W_j is found using the expression [12]:

$$W_j = \sqrt{\frac{2\varepsilon\varepsilon_0\varphi_b}{qN}} \quad (13)$$

$$\varphi_b = V_t ln \frac{N_d N_a}{{n_i}^2} \quad (14)$$

Where φ_b is the barrier (built-in) potential, N is the base doping level, n_i is the electron and hole concentration in undoped semiconductor material, N_d is donor atoms concentration, and N_a is acceptor atoms concentration. Thus the W_j will be much smaller than the W_i. Thus, the distance between p and n regions ($W = Wi + 2W_t$) dominates the parasitic resistance of the p-i-n structure.

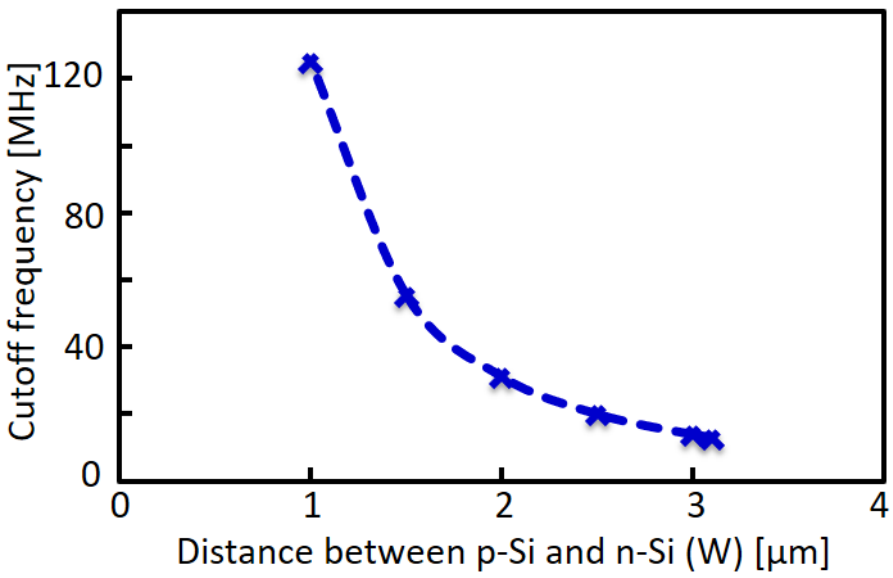

Fig. 20. Cutoff frequency as a function of width of the trench region. It shows that the smaller width will makes the cut-off frequency of the device higher.

By assuming that the only variable that changes just the W, while the doping condition just the same. Thus, the charge contrast region or the depletion area of I-Si and N-Si is assumed to remain the same. As the result, the frequency response can be calculated as the function of W. Figure 20 shows the dependence of cutoff frequency as the function of W. It shows that the narrower the W, the higher cutoff frequency of the device. However, to prevent radiation loss due to the optical coupling between the waveguide and p/n regions, W_t should not be too small. The minimum width of the waveguide, W_i should be at least 1/3 of the wavelength. Therefore, a minimum W of 1.5 µm can be realized by setting both W_t and W_i to 0.5 µm, resulting from the cutoff frequency of 55.5 MHz. while for the switching time, it can be improved to be 9 ns if this condition was applied to the device, as it is shown in Fig. 21.

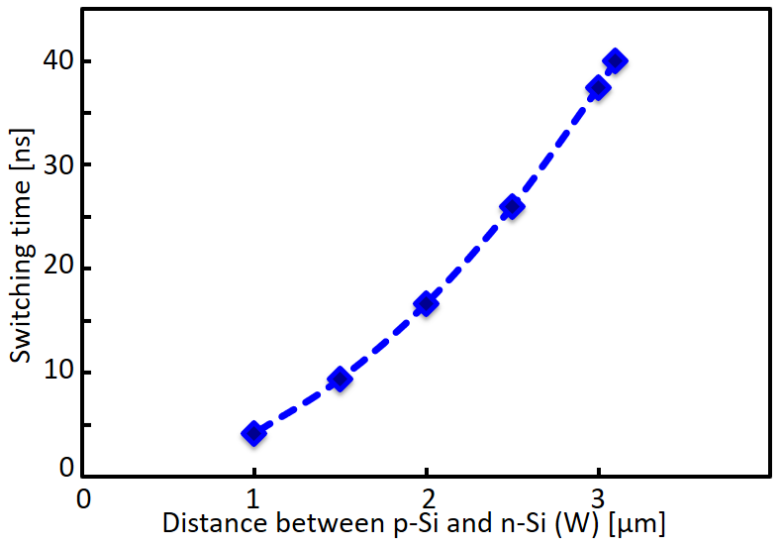

Fig. 21. Switching time as the function of Width of trench structure. The smaller width will decrease the resistance of the device, thus, the switching time will be faster.

In order to further improvement of the switching performance, increasing the capacitance of the p-i-n junction is also necessary. Since the capacitance is dependent to the cross section A and depletion layer (W_j), and the cross section of capacitance and Resistance are eliminating each other, then, the possible way to decrease the capacitance is by increase the depletion layer [12]. Since the depletion layer is dependent to the base doping level N. Thus, Increasing the doping level should be considered for both p-Si and n-Si region, while keeping in mind the effect on propagation loss [8].

The other way to improve the switching performance is by optimizing the diffusion of the doped Si in the trench p-i-n structure. According to the simulation by using SRIM, when the insulator layer of SiO_2 was also calculated into the simulation, the peak of concentration distribution moves to the surface area, as shown in Fig. 22. While to make the diffusion of the doped region distributed equally to the surface and inside the Si, the peak should be located in the central of the Si layer, in this case, the thickness of Si was 300 nm which makes the central area should be 150 nm depth. Thus, the higher implantation energy is needed to optimize the doped distribution inside the Si.

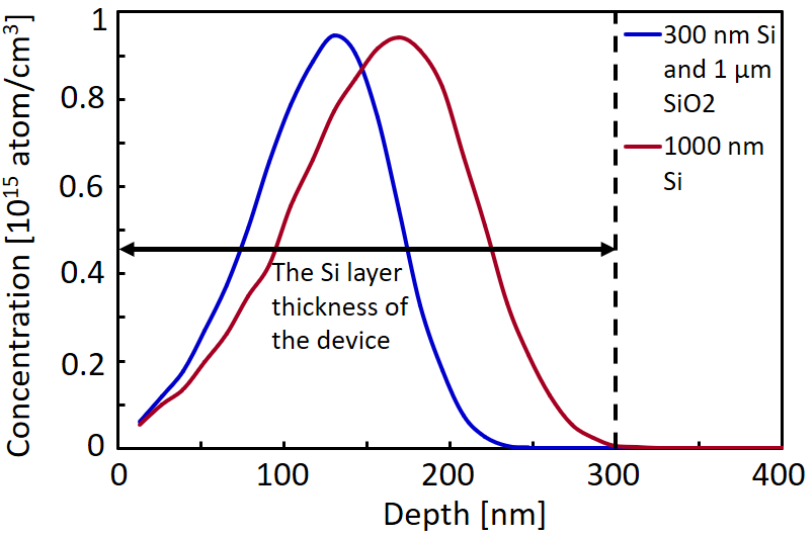

Fig. 22. Boron ions distribution inside the Si with and without insulator layer of SiO_2.

Since the current was injected from the surface of doped Si region of the p-type and n-type region, the total current that is needed to realize the π phase shifted is also dependent to the resistivity of the doped region. Since the resistivity of the doped Si is dependent into the doped concentration which is the higher concentration of the dopant, the lower resistivity of the doped Si [9]. Thus, the total resistance of the trench structure can be decreased by increasing the concentration of doped region as well. However, too high dose ion implantation can change the properties of the photoresist. As the dose level increases, the photoresist cannot be stripped off completely by chemical strippers, hot nitric acids, or hot sulfuric acids; the chemical durability and hardness of the resist films are increased [3, 10].

4.5 Conclusions

We proposed an optical mode switch and found the switching time by using p-i-n trench structure was 40 ns for the first-order mode to fundamental mode, and a switching time of 60 ns for the fundamental mode to the first-order mode. This switching time can be improved by optimizing the p-i-n trench structure as the main part to shift the phase of the fundamental mode in one of the arms. The improvement can be done by optimizing the trench dimension, increasing the dose level, and optimizing the implantation energy.

4.6 References

[1] J. F. Ziegler, "SRIM – The Stopping and Range of Ions in Matter," http://www.srim.org/ : accessed January 2018.

[2] Jones, S. W, "Diffusion in Silicon," ICKnowledge LLC, 2008. http://www-eng.lbl.gov/~shuman/NEXT/MATERIALS&COMPONENTS/Xe_damage/Diffusionin%20siliconpdf.pdf : accessed April 2018.

[3] Y. Okuyama, T. Hashimoto, and T. Koguchi, "High Dose Ion Implantation into Photoresist," J. Electrochem. Soc., vol. 125, no. 8, 1293-1298, Apr. 1978.

[4] R. Imansyah, T. Tanaka, L. Himbele, H. Jiang, and K. Hamamoto, "Electrically controlled optical-mode switch for fundamental mode and first order mode," Jpn. J. Appl. Phys., vol.55, 8S3, 2016.

[5] R. Imansyah, T. Tanaka, L. Himbele, H. Jiang, and K. Hamamoto, “Mode crosstalk evaluation on optical mode switch by using MMI mode filter,” IEICE Trans. Electron., vol.E99-C, no.7, pp.825–829, 2016.

[6] K. Yamada, “Silicon photonic wire waveguides: fundamentals and applications,” in Silicon Photonics II Components and Intergration ed. D.J. Lockwood, L. Pavesi, pp.1–29, Springer-Verlag Berlin Heidelberg, 2011.

[7] H. Jiang, R. Imansyah, L. Himbele, S. Oe, and K. Hamamoto, “Fast Mode-Switching (60 ns) by Using a 2×2 Silicon Optical Mode Switch,” IEICE Trans. Electron., vol.E100-C, no.10, pp.782–788, 2017.

[8] C.A. Barrios, V.R. Almeida, R. Panepucci, and M. Lipson, “Electrooptic modulation of silicon-on-insulator submicrometersize waveguide devices,” J. Lightwave Technol., vol.21, no.10, pp.2332–2339, 2003.

[9] P. W. Chapman, 0. N. Tufte, J. D. Zook, and D. Long, “Electrical properties of heavily doped silicon,” J. Appl. Phys., vol. 34, no. 11, pp. 3291-3295, Nov. 1963.

[10] S. Wang, J. Li, Y. Chen, D. Zhao, Y. Wang, and H. Zhang, “Removal of high dose ion-implanted photoresists using dry process,” ICEPT 18th, Sept. 2017

[11] R. P. Arias, “PIN Diode Switch Circuit for Short Time High Current Pulse Signal,” Master Thesis, Massachusetts Institute of Technology, June, 1998.

[12] I. V. Lebedev, A. S. Shnitnikov, I. V. Dyakov, and N. A. Borisova, “Impedance properties of high-frequency pin diodes,” Solid-State Electronics, Elsevier, vol. 42, issue 1, 121-128, Jan. 1998.

Chapter 5

Conclusions and outlook

5.1 Conclusions

As mentioned in Chap. 1, the optical mode switch is attractive to overcome the problems in switching due to the hardware limitations of electrical DCs. The optical mode switch is expected to realize the optical switching with three major properties of optical transmission technology: ultra-high capacity, low power consumption, and small footprint. Several optical mode switches were proposed, however, majority these mode switches suffer from low switching speed, high driving voltage, and large size.

In Chap. 2 the schematic of the optical mode switch is described. The configuration that is similar to that of a Mach-Zehnder interferometer with a difference in the waveguide width of the Y-junction connected to the two single-mode waveguides. The width of the waveguide at the Y-junction is designed to be twice of the arm's width to realize mode combining for the fundamental mode as well as the first-order mode. The symmetrical arms with a refractive index change region in one of the arms was fabricated in order to realize the mode switching. In this index change region, the electrical current was injected to generate a π-phase difference between arms. There are two parameters to optimize the optical propagation; the Y-junction Radius R and the p-i-n trench structure. The R of the device should be larger than 8 μm to avoid the radiation loss but small enough to keep the small footprint of the device. While in the p-i-n trench structure, the trench width of W_t should be small enough to make the remaining silicon layer thick enough to realize the ion plasma dispersion for phase shifting. The p-i-n

trench structure was realized by utilizing the aspect-ratio-dependent etching (ARDE) phenomenon. The experiment shows that by setting the open space as 0.8 µm, 30 nm silicon layer was remained as the connector of the waveguide to both the p-doped and n-doped regions after single-step dry etching, because of the etching rate difference.

In Chap. 3 we gave a brief explanation of mode evaluation method that we are using for the MMI mode filter. We were using the 1×3 MMI mode filter because there is only one input port for this MMI mode filter and no phase shifter is needed to make the MMI mode filter working. As a result, MMI mode filter with W_{MMI} of 10 µm and L_{MMI} of 208 µm shows the best mode crosstalk results. By integrating the MMI mode filter, a path difference device was integrated with the MMI mode filter to see the MMI mode filter performance over mode switching device. The result shows that the insertion loss of this device is approximate 20 dB with the crosstalk of approximately 10 dB. This MMI mode filter performance can be increased by applying the taper in the MMI coupler. Simulation result shows that the MMI mode filter with the taper width of 1 µm shows the best result of fabrication tolerance with only -10 dB/0.5 µm.

In Chap. 4 the mode-switching time of 2×2 silicon optical mode switch by using p-i-n trench structure was 40 ns for the first-order mode to the fundamental mode, and a switching time of 60 ns for the fundamental mode to first order mode. This switching time can be improved by optimizing the p-i-n trench structure as the main part to shift the phase of the fundamental mode in one of the arms. The improvement can be done by optimizing the trench dimension, increasing the dose level, and optimizing the implantation energy.

5.2 Outlook

We hope and believe that the optical mode switch will contribute to improving the performance of the data center to support the very large scales of internet traffic while also keep the footprint and lower the power consumption. Although the propagation loss was quite high and the current was not low enough, the switching speed was 40 ns and 60 ns. The performance can be improved by optimizing the fabrication process.

Appendix

List of symbol

A	The dopant atoms
C	Capacitance
C_i	Capacitance of undepleted area
C_j	Capacitance of depleted area
C_V	The dopant concentration per unit volume
D	The diffusion coefficient of diffusivity
D_c	The dispersion constant
Δn	Change in the refractive index
Δn_h	Change in the refractive index because of the change in free hole carrier concentration
Δn_e	Change in the refractive index because of the change in free electron carrier concentration
ΔN_e	The change in free electron carrier concentration
ΔN_h	The change in free hole carrier concentration

f_c	Cut-off frequency
h_s	The thickness of the remaining Si layer in trench region
I_F	The forward bias current
i-Si	Intrinsic Silicon
J	The number of dopant atoms
k	Wavenumber
μ	The mobility of carriers in the intrinsic region
N	The base doping level
N_a	Acceptor atoms concentration
N_d	Donor atoms concentration
n_i	The electron and hole concentration in undoped semiconductor material
n-Si	Silicon with Phosphorus doped
p-Si	Silicon with Boron doped
ϕ	The guided modes number in MMI
φ_b	The barrier (built-in) potential
R	Resistance
r	Radius

R_f	Resistance of PIN diode
Rp	The peak depth of dopant
ω	Frequency
S	The cross section area
τ	The carrier lifetime
u	The guided modes number in MMI
W_t	The trench width of trench region
x	The depth of the semiconductor
W	Width of the intrinsic part of PIN structure
W_i	Width of the undepleted area of PIN structure
W_j	Width of the depleted area of PIN structure

List of abbreviations

ARDE	The aspec-ratio-dependent-etching
BGA	Ball grid array
BPM	Beam propagation method
DC	Data Center
DSP	Digital signal processing
EB	Exabytes
EDFA	Erbium-doped fiber-amplifiers
FDTD	Finite domain time difference
FMF	Few-mode fiber
ICP	Inductive coupled plasma
IP	Internet Protocol
MCF	Multi-core fiber
MDM	Mode division multiplexing
MEMS	Micro-electro-mechanical systems
MIMO	Multi-input multi-output

MMF	Multi-mode fiber
MMI	Multimode interference
NFP	Near-field apattern
OEO	optica-electrical-optical
SDM	Spatial division multiplexing
SOI	Silicon-on-insulator
TDM	Time division multiplexing
TE	Transverse electric
ToR	Top-of-rack
WDM	Wavelength division multiplexing
ZB	Zettabytes